An SVPWM Strategy With Extended Linear Modulation Range for Dual Three-Phase Machine Drives Under Unbalanced Power Sharing Conditions

Xiaochen Ma, Bin Li, Guidan Li, and Qiaoman Zhu

***Abstract*—In this article, a new space vector pulsewidth modulation (SVPWM) strategy is proposed for dual three-phase (DTP) machine drives. The proposed strategy is based on vector space decomposition (VSD) and mainly targets the scenario where power of the two subthree-phase winding sets of the machine is unequal. In the basic VSD-based SVPWM strategies, the constraints of nonnegative dwell time of the basic vectors result in zero linear modulation range when the DTP machine is under unbalanced power sharing conditions. Different from them, this article investigates the maximum linear modulation capability of VSD-based SVPWM under power sharing by removing the dwell time constraints of the basic vectors. In this regard, only the physical limitations of the dwell time of each phase need to be guaranteed. According to this principle, a two-step-based design procedure of the proposed modulation strategy is presented in detail, followed by a numerical analysis regarding its linear modulation boundary. Moreover, the performance comparisons with many other typical VSD-based SVPWM strategies are also conducted. It has been theoretically and experimentally proven that the proposed SVPWM solution can obtain maximum linear modulation range when the DTP machine is under unbalanced power sharing.**

***Index Terms*—Dual three-phase machine, linear modulation, power sharing, space vector pulsewidth modulation, vector space decomposition.**

I. Introduction

MULTITHREE-PHASE machines that possess multiple subthree-phase winding sets exhibit outstanding merits, such as reduced current ratings, lower torque ripples, higher control flexibility, as well as enhanced fault-tolerant capability over their conventional three-phase counterparts [1], [2]. Nowadays, they have already played a crucial role for applications in wind generations, electric propulsion systems, and so on [3], [4].

Manuscript received 28 June 2023; revised 30 September 2023 and 21 November 2023; accepted 23 December 2023. Date of publication 26 December 2023; date of current version 16 February 2024. This work was supported by the Tianjin Research Innovation Project for Postgraduate Students under Grant 2022BKY067. Recommended for publication by Associate Editor D. Lee. *(Corresponding author: Bin Li.)*

Xiaochen Ma, Bin Li, and Guidan Li are with the School of Electrical and Information Engineering, Tianjin University, Tianjin 300072, China (e-mail: maxc@tju.edu.cn; elib@tju.edu.cn; lgdtju@tju.edu.cn).

Qiaoman Zhu is with Jianghuai Advance Technology Center, Hefei 230088, China (e-mail: qiaoman_0121@tju.edu.cn).

Color versions of one or more figures in this article are available at https://doi.org/10.1109/TPEL.2023.3347304.

Digital Object Identifier 10.1109/TPEL.2023.3347304

In multithree-phase machine drives, an interesting feature is to control the current in each subthree-phase winding set independent of that in other subthree-phase winding sets, which is hereinafter referred to as "power sharing". First, for series-connected bus structure, utilizing the unbalanced power of different subthree-phase winding sets of the machine can compensate for the imbalance of bus power, thereby achieving bus voltage equalization [5], [6]. Second, when different subthree-phase winding sets of the machine are fed by independent energy sources, the power sharing control of machine can result in the power regulation among different energy sources. Hence, in addition to realizing the inherent electromechanical energy conversion function of machine, it can also be regarded as an effective way to achieve optimal energy management in multiple energy sources system without the need for additional power converters [6], [7], [8]. Third, by setting half of the subthree-phase winding sets to the motoring state and the remaining subthree-phase winding sets to the generation state, the active power can be circulated among different subthree-phase winding sets, thus achieving load testing without the need for additional load machine [9], [10]. From the potential values of the abovementioned three aspects, it can be seen that the research on power sharing control for multithree-phase machine drives is of great significance.

For multithree-phase machine modeling, multistator (MS) and vector space decomposition (VSD) are two representative methodologies [11]. In MS model, the standard three-phase Clarke and Park transformations are applied to each subthree-phase winding set individually. Hence, the power sharing information of the machine is intuitive. Nonetheless, there is an issue of magnetic coupling among different winding sets in this model, which may lead to potential instability [12]. On the contrary, VSD is a decoupled modeling method due to the introduction of several mutually orthogonal subspaces (i.e., fundamental subspace and harmonic subspaces) [13]. As a result, stability and robustness of the drive system can be promoted [12]. Under VSD modeling, the mechanism to achieve power sharing of multithree-phase machine has also been recognized [6], [14]. Specifically, the unbalanced power among different subthree-phase winding sets can be regulated by setting appropriate reference currents/voltages in each harmonic subspace, while the reference currents/voltages in fundamental subspace reflect the total power production.

Relying on the advantages of VSD, currently, various types of VSD-based space vector pulsewidth modulation (SVPWM) strategies have been studied for dual three-phase (DTP) machine drives. The VSD-based four-active-vector-type (VSD-4V) SVPWM is widely employed to deal with the DTP machines with two isolated neutral points. According to the vector length difference in fundamental subspace, options for selecting such four active vectors include the 4L method [13], the 2L+2ML method [15], some 2L+1ML+1M methods [16], and some 3L+1M methods [16], [17], where L, ML, and M represent large vector, medium-large vector, and medium vector, respectively. These specific implementation methods of VSD-4V SVPWM have characteristic differences within the switching cycle, but the linear modulation ranges are completely the same [16], [17], [18]. In addition to the basic VSD-4V SVPWM, many modified VSD-based SVPWM strategies have also been explored to suppress the common-mode voltage [19], reduce the harmonic distortion factor [20], PWM current harmonics [21], or address the issues caused by unbalanced dc bus voltages [22].

Regarding all the aforementioned VSD-based SVPWM strategies, a common feature is that the amplitude of the reference voltage vector (RVV) in harmonic subspace is zero. However, in the case of harmonic suppression, this is not the optimal solution since nonzero harmonic injection is often required to offset the original harmonic components [23], [24], [25]. Thus, it is best for the SVPWM to have linear modulation capability of nonzero RVV in harmonic subspace (i.e., not only in fundamental subspace). Unfortunately, as analyzed in [26], once the amplitude of the harmonic subspace RVV becomes nonzero, the basic VSD-4V SVPWM will have zero linear modulation range. To compensate for this deficiency, the idea of splitting the modulation into two independent stages per PWM cycle is proposed in [25]. Specifically, the first modulation stage selects four active vectors to synthesize the nonzero RVV in fundamental subspace, while the second modulation stage reselects four active vectors to synthesize the nonzero RVV in harmonic subspace. Thanks to the complete decoupling of the two stages, both subspaces can achieve linear modulation under nonzero RVVs. Nevertheless, the doubled modulation stage in this approach leads to undesired multiple switching. To avoid such issue, in [26], an optimization method is further provided by generating the equivalent single pulse for each inverter phase within a PWM cycle. In summary, owing to the capability in linearly modulating nonzero RVVs in both fundamental and harmonic subspaces, the two-modulation-stage-based SVPWM strategies proposed in [25] and [26] are good candidates for DTP machine drives with harmonic regulation requirements.

As aforementioned, unbalanced power sharing of the DTP machine can be achieved by setting nonzero voltage commands in both fundamental and harmonic subspaces. Therefore, in essence, as long as the SVPWM strategy can achieve nonzero RVV linear modulation in both subspaces (such as those in [25] and [26]), it can be then applied to power sharing conditions. Nonetheless, with regard to the existing SVPWM techniques and their corresponding analysis, two main problems can still be found as follows.

1) For VSD-based SVPWM strategies with nonzero RVV modulation in both fundamental and harmonic subspaces, whether the linear modulation range can be further extended is not clear.
2) Although power sharing control and harmonic regulation both belong to nonzero RVV modulation in fundamental and harmonic subspaces, there are still significant differences in frequency feature of the harmonic subspace RVV in these two scenarios. Due to neglecting the impact of RVV frequency feature, conventional methods for solving the linear modulation boundary in harmonic regulation scenario will not be suitable for evaluating the real linear modulation boundary in power sharing control scenario.

To this end, aiming at DTP machine drives, a new SVPWM strategy suitable for power sharing conditions is studied in this article. The main contributions of the proposal are as follows.

1) A new modulation method based on allowing negative dwell time of the basic vectors is proposed for VSD framework. By this way, the achievable direction of nonzero vector synthesis becomes arbitrary, thereby creating the capability of nonzero RVV linear modulation in both fundamental and harmonic subspaces.
2) When nonzero RVV exists in both fundamental and harmonic subspaces, a more accurate method for solving the linear modulation boundary is investigated. Different from the conventional analysis methods, the proposed method fully considers the frequency feature of the RVV, thereby excavating more potential regions for achieving linear modulation.
3) Compared with the existing SVPWM strategies that also have nonzero RVV linear modulation capability in both fundamental and harmonic subspaces, the proposed SVPWM strategy can achieve maximum linear modulation range under unbalanced power sharing conditions.

The rest of this article is organized as follows. Section II analyzes the model and vector features of DTP machine drives under power sharing. In Section III, the design idea of the proposed strategy and the analysis of its linear modulation boundary are demonstrated, followed by the comparisons with many other strategies. Experimental results are presented in Section IV. Finally, Section V concludes this article.

II. Model and Vector Analyses of DTP Machine Drives Under Power Sharing

A. Model of DTP Machine Under Power Sharing

Fig. 1 shows the studied drive system, where the machine has two subthree-phase winding sets (ABC and DEF) with $\pi/6$ spatial shift angle [12]. By the VSD transformation matrix in [27], the phase variables of the DTP machine can be mapped into three orthogonal subspaces, namely $\alpha\beta$ subspace, xy subspace, and $o1o2$ subspace. For the studied machine, $o1o2$ subspace can be ignored due to isolated neutral points.

To analyze power sharing of DTP machine, by applying the 0 and $\pi/6$ phase shifted Clarke transformation matrices in [27] to ABC and DEF sets, respectively, the relation between VSD

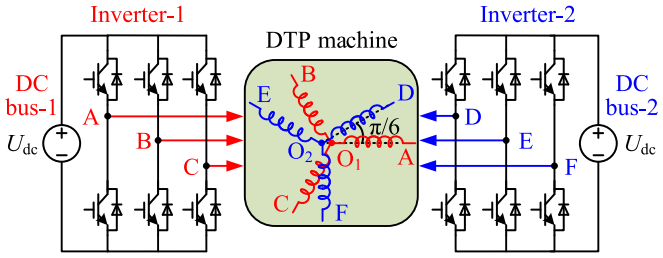

Fig. 1. Voltage source inverter fed DTP machine drive system.

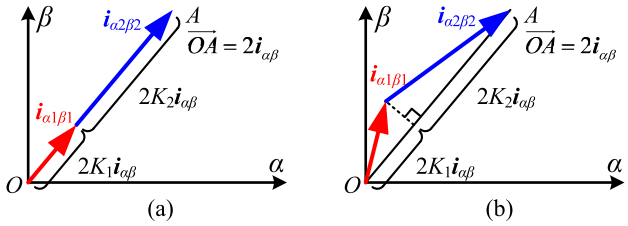

Fig. 2. Current vectors $\boldsymbol{i}_{\alpha1\beta1}$ and $\boldsymbol{i}_{\alpha2\beta2}$ under power sharing. (a) $\boldsymbol{i}_{\alpha1\beta1}$ and $\boldsymbol{i}_{\alpha2\beta2}$ are aligned. (b) $\boldsymbol{i}_{\alpha1\beta1}$ and $\boldsymbol{i}_{\alpha2\beta2}$ are not aligned.

variables and two subthree-phase variables can be obtained as

$$\boldsymbol{F}_{\alpha\beta} = 0.5(\boldsymbol{F}_{\alpha1\beta1}+\boldsymbol{F}_{\alpha2\beta2}), \quad \boldsymbol{F}_{xy} = 0.5(\boldsymbol{F}_{\alpha1\beta1}-\boldsymbol{F}_{\alpha2\beta2})^* \tag{1}$$

where $\alpha1\beta1$ and $\alpha2\beta2$ denote the stationary reference frame of the first subthree-phase winding set and second subthree-phase winding set, respectively; the vector $\boldsymbol{F}$ can be voltage u, current i, and flux ψ; "*" means complex conjugate operation.

For DTP machine under power sharing, Fig. 2 shows two different types of current vectors in the first subthree-phase winding set ($\boldsymbol{i}_{\alpha1\beta1}$) and second subthree-phase winding set ($\boldsymbol{i}_{\alpha2\beta2}$). $\boldsymbol{i}_{\alpha1\beta1}$ and $\boldsymbol{i}_{\alpha2\beta2}$ are aligned in Fig. 2(a), while they are not aligned in Fig. 2(b). As the total power is solely determined by the VSD current $\boldsymbol{i}_{\alpha\beta}$, the vector sum of $\boldsymbol{i}_{\alpha1\beta1}$ and $\boldsymbol{i}_{\alpha2\beta2}$ ($= 2\boldsymbol{i}_{\alpha\beta}$) needs to remain unchanged (i.e., $\overrightarrow{OA}$ in Fig. 2) according to (1). Hence, if K_1: K_2 (K_1+K_2 = 1) is the required power sharing ratio of the two subthree-phase winding sets, it means that the projection ratio of $\boldsymbol{i}_{\alpha1\beta1}$ and $\boldsymbol{i}_{\alpha2\beta2}$ on $\overrightarrow{OA}$ should be K_1: K_2.

Under this premise, Fig. 2(a) and (b) will result in the same total power and power sharing ratio. However, the amplitudes of $\boldsymbol{i}_{\alpha1\beta1}$ and $\boldsymbol{i}_{\alpha2\beta2}$ in Fig. 2(a) are evidently the minimal. Thus, to achieve power sharing with minimum copper loss, $\boldsymbol{i}_{\alpha1\beta1}$ and $\boldsymbol{i}_{\alpha2\beta2}$ should be controlled as in Fig. 2(a), which yields

$$\boldsymbol{i}_{\alpha1\beta1} = 2K_1 \cdot \boldsymbol{i}_{\alpha\beta}, \quad \boldsymbol{i}_{\alpha2\beta2} = 2K_2 \cdot \boldsymbol{i}_{\alpha\beta}. \tag{2}$$

From the above analysis, two conclusions can be drawn as follows.

1) Based on (1), $\boldsymbol{i}_{xy}$ will be nonzero as long as $\boldsymbol{i}_{\alpha1\beta1} \neq \boldsymbol{i}_{\alpha2\beta2}$ for power sharing. Moreover, even under power sharing, both $\boldsymbol{i}_{\alpha1\beta1}$ and $\boldsymbol{i}_{\alpha2\beta2}$ still need to rotate counterclockwise at the fundamental frequency to achieve circular rotational magnetomotive force (MMF). So, (1) indicates that $\boldsymbol{i}_{\alpha\beta}$ and $\boldsymbol{i}_{xy}$ will rotate at the fundamental frequency, but their directions are counterclockwise and clockwise, respectively.
2) If power sharing is expected to be achieved with minimum copper loss, by combining (1) and (2), the nonzero $\boldsymbol{i}_{xy}$ should further have the following features:

$$i_x = (K_1 - K_2)i_\alpha, \quad i_y = (-K_1 + K_2)i_\beta. \tag{3}$$

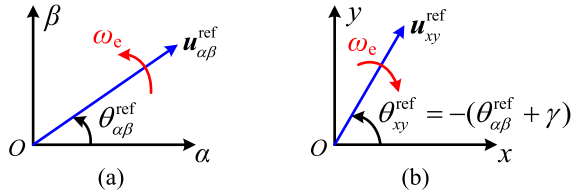

Fig. 3. RVVs of DTP machine drives under power sharing. (a) $\alpha\beta$ subspace. (b) xy subspace.

B. RVVs Under Power Sharing

As analyzed in Section II-A, no matter minimum copper loss is required or not, both $\boldsymbol{i}_{\alpha\beta}$ and $\boldsymbol{i}_{xy}$ will be nonzero under power sharing. To realize the required rotation features of $\boldsymbol{i}_{\alpha\beta}$ and $\boldsymbol{i}_{xy}$, the RVV in $\alpha\beta$ subspace ($\boldsymbol{u}_{\alpha\beta}^{ref}$) and the RVV in xy subspace ($\boldsymbol{u}_{xy}^{ref}$) should also be nonzero and rotate at the fundamental frequency ω_e, with their directions being counterclockwise and clockwise, respectively.

Fig. 3 shows the RVVs in both $\alpha\beta$ and xy subspaces under power sharing. To describe the phase relationship of $\boldsymbol{u}_{\alpha\beta}^{ref}$ (phase angle is $\theta_{\alpha\beta}^{ref}$) and $\boldsymbol{u}_{xy}^{ref}$ (phase angle is θ_{xy}^{ref}), the phase angle difference γ (constant value) can be introduced as

$$\gamma = -(\theta_{\alpha\beta}^{ref} + \theta_{xy}^{ref}). \tag{4}$$

Subsequently, u_α^{ref}, u_β^{ref}, u_x^{ref}, and u_y^{ref} can be represented as

$$\begin{cases} u_\alpha^{ref} = \left\|\boldsymbol{u}_{\alpha\beta}^{ref}\right\| \cos\theta_{\alpha\beta}^{ref}, \quad u_\beta^{ref} = \left\|\boldsymbol{u}_{\alpha\beta}^{ref}\right\| \sin\theta_{\alpha\beta}^{ref} \\ u_x^{ref} = \left\|\boldsymbol{u}_{xy}^{ref}\right\| \cos(\theta_{\alpha\beta}^{ref} + \gamma), \quad u_y^{ref} = -\left\|\boldsymbol{u}_{xy}^{ref}\right\| \sin(\theta_{\alpha\beta}^{ref} + \gamma). \end{cases} \tag{5}$$

C. Model of DTP Voltage Source Inverter

The DTP inverter presented in Fig. 1 is responsible for modulating the RVVs in $\alpha\beta$ and xy subspaces. The voltage of both dc buses is U_{dc}. Under VSD model, the DTP inverter generates totally $2^6 = 64$ basic vectors, including 60 active vectors and four zero vectors. The active vectors can be classified into four categories with lengths of $0.6440U_{dc}$ (large, L), $0.4714U_{dc}$ (medium-large, ML), $0.3333U_{dc}$ (medium, M), and $0.1725U_{dc}$ (small, S). Fig. 4 shows the distribution of the basic active vectors in $\alpha\beta$ and xy subspaces. All vectors are represented by the equivalent decimal numbers of the 6-bit binary numbers "$S_FS_ES_DS_CS_BS_A$", where $S_A, \ldots, S_F$ are the switching states (1: upper switch is ON, 0: lower switch is ON) of phases A, …, F, respectively. The black labels 1−12 represent the sector numbers $N_{\alpha\beta}$ and N_{xy} of $\alpha\beta$ subspace and xy subspace, respectively.

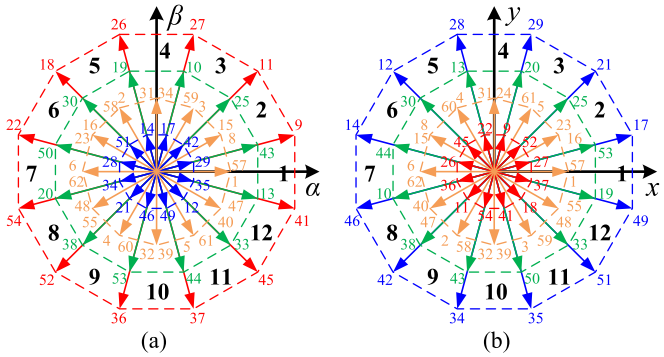

Fig. 4. Basic active voltage vector distribution of DTP voltage source inverter. (a) $\alpha\beta$ subspace. (b) xy subspace.

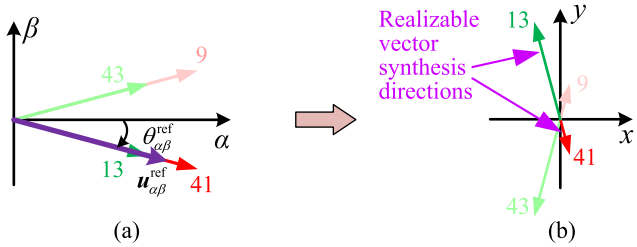

Fig. 5. Vector synthesis of the basic VSD-4V strategy when $\theta_{\alpha\beta}^{\text{ref}} = -\pi/12$. (a) $\alpha\beta$ subspace. (b) xy subspace.

III. Proposed VSD-Based SVPWM Strategy

A. Basic Idea

As pointed out in Section I, the basic VSD-4V SVPWM strategies do not have nonzero RVV linear modulation capability in harmonic (xy) subspace. By taking the 2L+2ML vector selection method as an example, the specific vector synthesis feature of the basic strategy can be analyzed in Fig. 5. When $\theta_{\alpha\beta}^{\text{ref}} = -\pi/12$, the four active vectors 43, 9, 41, and 13 should be selected. Due to the non-negative constraints of the vector dwell time, one can find from Fig. 5(a) that the dwell times of vectors 43 and 9 need to be zero to synthesize $\boldsymbol{u}_{\alpha\beta}^{\text{ref}}$. Thus, as indicated in Fig. 5(b), the achievable vector synthesis directions in xy subspace are only the directions of vectors 41 and 13. If the actual direction of $\boldsymbol{u}_{xy}^{\text{ref}}$ is not consistent with the vectors 41 or 13, then the modulation of $\boldsymbol{u}_{xy}^{\text{ref}}$ will fail.

From the abovementioned analysis, one can consider that the reason for modulation failure in xy subspace is the lack of capability to synthesize nonzero vector with arbitrary directions. Hence, the main objective of this article is to find a way to broaden the feasible direction of the nonzero vector synthesis in xy subspace.

Still taking $\theta_{\alpha\beta}^{\text{ref}} = -\pi/12$ as the example, the basic idea of the proposed SVPWM strategy is demonstrated in Fig. 6. Different from the conventional principle, this article removes the non-negative constraints of the vector dwell time. Thus, as depicted in Fig. 6(a), it can be considered that the candidate active vectors include not only the original vectors 43, 9, 41, and 13, but also their opposite vectors 20, 54, 22, and 50 if negative

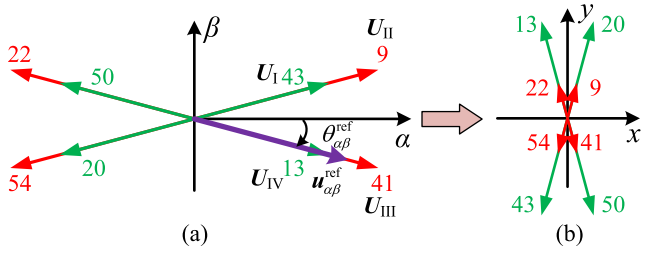

Fig. 6. Vector synthesis of the proposed strategy when $\theta_{\alpha\beta}^{\text{ref}} = -\pi/12$. (a) $\alpha\beta$ subspace. (b) xy subspace.

dwell time occurs. In this case, the RVV in $\alpha\beta$ subspace ($\boldsymbol{u}_{\alpha\beta}^{\text{ref}}$) can be synthesized by various dwell time combinations from these eight vectors (dwell times of vectors 43, 9, 20, and 54 can be nonzero as long as these vectors do not produce components perpendicular to $\boldsymbol{u}_{\alpha\beta}^{\text{ref}}$). Consequently, as shown in Fig. 6(b), the achievable vector synthesis directions in xy subspace have more selectivity.

Furthermore, it is worth noting that the proposed strategy without non-negative dwell time constraints still only needs to select four original basic vectors (e.g., vectors 43, 9, 41, and 13 when $-\pi/12 \le \theta_{\alpha\beta}^{\text{ref}} < \pi/12$) by the sector judgment on $\boldsymbol{u}_{\alpha\beta}^{\text{ref}}$. When the calculation shows that the dwell time of an original vector should be negative to synthesize $\boldsymbol{u}_{\alpha\beta}^{\text{ref}}$ and $\boldsymbol{u}_{xy}^{\text{ref}}$, applying the negative dwell time to the original vector is equivalent to applying the same positive dwell time to the corresponding opposite vector. Therefore, the proposed strategy can be achieved without changing the dwell time expressions of the basic vectors. As a consequence, in practical implementation, the toggling point of applying either the original vector or the opposite vector does not require prior judgment.

B. Design Procedure of the Proposed SVPWM Strategy

In light of the potential advantages by allowing negative dwell time of the basic vectors, a two-step-based design procedure is presented in this section to form the complete version of the proposed SVPWM strategy.

1) Step-1: Cancel the Non-Negative Dwell Time Constraints of Each Basic Vector: This step selects two L active vectors and two ML active vectors in $\alpha\beta$ subspace adjacent to $\boldsymbol{u}_{\alpha\beta}^{\text{ref}}$ as the starting point. The two original selected ML vectors are defined as $\boldsymbol{U}_{\text{I}}$ and $\boldsymbol{U}_{\text{IV}}$ in this article, while the two original selected L vectors are defined as $\boldsymbol{U}_{\text{II}}$ and $\boldsymbol{U}_{\text{III}}$. For instance, when $-\pi/12 \le \theta_{\alpha\beta}^{\text{ref}} < \pi/12$, based on Fig. 6(a), $\boldsymbol{U}_{\text{I}}$, $\boldsymbol{U}_{\text{II}}$, $\boldsymbol{U}_{\text{III}}$, and $\boldsymbol{U}_{\text{IV}}$ are vectors 43, 9, 41, and 13, respectively. According to volt-second principle, the dwell times of $\boldsymbol{U}_{\text{I}}$–$\boldsymbol{U}_{\text{IV}}$ (T_{I}–T_{IV}) and the dwell time of zero vector (T_{zero}) can be calculated by

$$\begin{bmatrix} U_{\text{I}\alpha} & U_{\text{II}\alpha} & U_{\text{III}\alpha} & U_{\text{IV}\alpha} & 0 \\ U_{\text{I}\beta} & U_{\text{II}\beta} & U_{\text{III}\beta} & U_{\text{IV}\beta} & 0 \\ U_{\text{I}x} & U_{\text{II}x} & U_{\text{III}x} & U_{\text{IV}x} & 0 \\ U_{\text{I}y} & U_{\text{II}y} & U_{\text{III}y} & U_{\text{IV}y} & 0 \\ 1 & 1 & 1 & 1 & 1 \end{bmatrix} \begin{bmatrix} T_{\text{I}} \\ T_{\text{II}} \\ T_{\text{III}} \\ T_{\text{IV}} \\ T_{\text{zero}} \end{bmatrix} = T_{\text{PWM}} \begin{bmatrix} u_{\alpha}^{\text{ref}} \\ u_{\beta}^{\text{ref}} \\ u_{x}^{\text{ref}} \\ u_{y}^{\text{ref}} \\ 1 \end{bmatrix} \quad (6)$$

where T_{PWM} is the PWM cycle; $U_{i\alpha}$, $U_{i\beta}$, U_{ix}, and U_{iy} are the projections of $\boldsymbol{U}_i$ (i = I, II, III, IV) on α-, β-, x-, and y-axis, respectively.

When $\boldsymbol{u}_{\alpha\beta}^{\mathrm{ref}}$ lies in the first sector of $\alpha\beta$ subspace (i.e., $N_{\alpha\beta}=1$, $-\pi/12\le\theta_{\alpha\beta}^{\mathrm{ref}}<\pi/12$), by labeling $u_{\alpha}^{\mathrm{ref}}$, u_{β}^{ref}, u_{x}^{ref}, and u_{y}^{ref} as $u_{\alpha\_\mathrm{s1}}^{\mathrm{ref}}$, $u_{\beta\_\mathrm{s1}}^{\mathrm{ref}}$, $u_{x\_\mathrm{s1}}^{\mathrm{ref}}$, and $u_{y\_\mathrm{s1}}^{\mathrm{ref}}$, respectively, T_{I}–T_{IV} and T_{zero} can be given as

$$\begin{cases} T_{\mathrm{I}}=\frac{\sqrt{3}T_{\mathrm{PWM}}}{2U_{\mathrm{dc}}}\begin{bmatrix}(2-\sqrt{3})u_{\alpha\_\mathrm{s1}}^{\mathrm{ref}}+u_{\beta\_\mathrm{s1}}^{\mathrm{ref}}\\ -(2+\sqrt{3})u_{x\_\mathrm{s1}}^{\mathrm{ref}}-u_{y\_\mathrm{s1}}^{\mathrm{ref}}\end{bmatrix}\\ T_{\mathrm{II}}=\frac{\sqrt{3}T_{\mathrm{PWM}}}{2U_{\mathrm{dc}}}\begin{bmatrix}(\sqrt{3}-1)u_{\alpha\_\mathrm{s1}}^{\mathrm{ref}}+(1+\sqrt{3})u_{\beta\_\mathrm{s1}}^{\mathrm{ref}}\\ +(1+\sqrt{3})u_{x\_\mathrm{s1}}^{\mathrm{ref}}+(\sqrt{3}-1)u_{y\_\mathrm{s1}}^{\mathrm{ref}}\end{bmatrix}\\ T_{\mathrm{III}}=\frac{\sqrt{3}T_{\mathrm{PWM}}}{2U_{\mathrm{dc}}}\begin{bmatrix}(\sqrt{3}-1)u_{\alpha\_\mathrm{s1}}^{\mathrm{ref}}-(1+\sqrt{3})u_{\beta\_\mathrm{s1}}^{\mathrm{ref}}\\ +(1+\sqrt{3})u_{x\_\mathrm{s1}}^{\mathrm{ref}}-(\sqrt{3}-1)u_{y\_\mathrm{s1}}^{\mathrm{ref}}\end{bmatrix}\\ T_{\mathrm{IV}}=\frac{\sqrt{3}T_{\mathrm{PWM}}}{2U_{\mathrm{dc}}}\begin{bmatrix}(2-\sqrt{3})u_{\alpha\_\mathrm{s1}}^{\mathrm{ref}}-u_{\beta\_\mathrm{s1}}^{\mathrm{ref}}\\ -(2+\sqrt{3})u_{x\_\mathrm{s1}}^{\mathrm{ref}}+u_{y\_\mathrm{s1}}^{\mathrm{ref}}\end{bmatrix}\\ T_{\mathrm{zero}}=T_{\mathrm{PWM}}\left[1-\frac{\sqrt{3}}{U_{\mathrm{dc}}}(u_{\alpha\_\mathrm{s1}}^{\mathrm{ref}}-u_{x\_\mathrm{s1}}^{\mathrm{ref}})\right]. \end{cases} \tag{7}$$

For $\boldsymbol{u}_{\alpha\beta}^{\mathrm{ref}}$ in any sector 1–12 of $\alpha\beta$ subspace, according to the vector distribution shown in Fig. 4, T_{I}, T_{II}, T_{III}, T_{IV}, and T_{zero} can be obtained by substituting (8) into (7)

$$\begin{cases} u_{\alpha\_\mathrm{s1}}^{\mathrm{ref}}=u_{\alpha}^{\mathrm{ref}}\cos[(N_{\alpha\beta}-1)\cdot\frac{\pi}{6}]+u_{\beta}^{\mathrm{ref}}\sin[(N_{\alpha\beta}-1)\cdot\frac{\pi}{6}]\\ u_{\beta\_\mathrm{s1}}^{\mathrm{ref}}=-u_{\alpha}^{\mathrm{ref}}\sin[(N_{\alpha\beta}-1)\cdot\frac{\pi}{6}]+u_{\beta}^{\mathrm{ref}}\cos[(N_{\alpha\beta}-1)\cdot\frac{\pi}{6}]\\ u_{x\_\mathrm{s1}}^{\mathrm{ref}}=u_{x}^{\mathrm{ref}}\cos[(N_{\alpha\beta}-1)\cdot\frac{5\pi}{6}]+u_{y}^{\mathrm{ref}}\sin[(N_{\alpha\beta}-1)\cdot\frac{5\pi}{6}]\\ u_{y\_\mathrm{s1}}^{\mathrm{ref}}=-u_{x}^{\mathrm{ref}}\sin[(N_{\alpha\beta}-1)\cdot\frac{5\pi}{6}]+u_{y}^{\mathrm{ref}}\cos[(N_{\alpha\beta}-1)\cdot\frac{5\pi}{6}]. \end{cases} \tag{8}$$

By taking $\|\boldsymbol{u}_{\alpha\beta}^{\mathrm{ref}}\|=0.4U_{\mathrm{dc}}$, $\|\boldsymbol{u}_{xy}^{\mathrm{ref}}\|=0.15U_{\mathrm{dc}}$, and $\gamma=\pi/4$ as an example, Fig. 7 shows the resulted T_{I}–T_{IV} and T_{zero} by Step-1. The vector angle $\theta_{\alpha\beta}^{\mathrm{ref}}$ of $\boldsymbol{u}_{\alpha\beta}^{\mathrm{ref}}$ is ranged from 0 to 2 rad. As can be seen, except for zero vector, all active vectors exhibit negative dwell times within a partial interval of $\theta_{\alpha\beta}^{\mathrm{ref}}$.

Compared with the conventional SVPWM, another significant difference occurred by Step-1 is that the dwell time of each vector no longer varies periodically in each $N_{\alpha\beta}$ sector. Instead, the periodic variation of the vector dwell time is only reflected within the odd sectors ($N_{\alpha\beta}=1,3,\ldots,11$) or within the even sectors ($N_{\alpha\beta}=2,4,\ldots,12$). In Fig. 7, T_{zero} of the even $N_{\alpha\beta}$ sectors is lower than that of the odd sectors, so the even sectors represent the high modulation depth stage, while the odd sectors are the low modulation depth stage. In this regard, a more detailed analysis will be explained in Section III-C.

2) Step-2: Average the Dwell Time of Center Zero Vector and Edge Zero Vector: After obtaining T_{I}–T_{IV} and T_{zero} through Step-1, this step considers the generation of the dwell times T_{A}–T_{F} of phases A–F (upper switches). Conventionally, the relationship between T_i (i = A, B, C, D, E, F) and T_{I}–T_{IV} and T_{zero} can be shown as

$$T_i=T_{\mathrm{I}}\cdot S_{\mathrm{I}\_i}+T_{\mathrm{II}}\cdot S_{\mathrm{II}\_i}+T_{\mathrm{III}}\cdot S_{\mathrm{III}\_i}+T_{\mathrm{IV}}\cdot S_{\mathrm{IV}\_i}+T_{\mathrm{zero}}/2 \tag{9}$$

where S_{I_i}, S_{II_i}, S_{III_i}, and S_{IV_i} are the switching states S_i (= 1 or 0) of the basic vectors $\boldsymbol{U}_{\mathrm{I}}$, $\boldsymbol{U}_{\mathrm{II}}$, $\boldsymbol{U}_{\mathrm{III}}$, and $\boldsymbol{U}_{\mathrm{IV}}$, respectively.

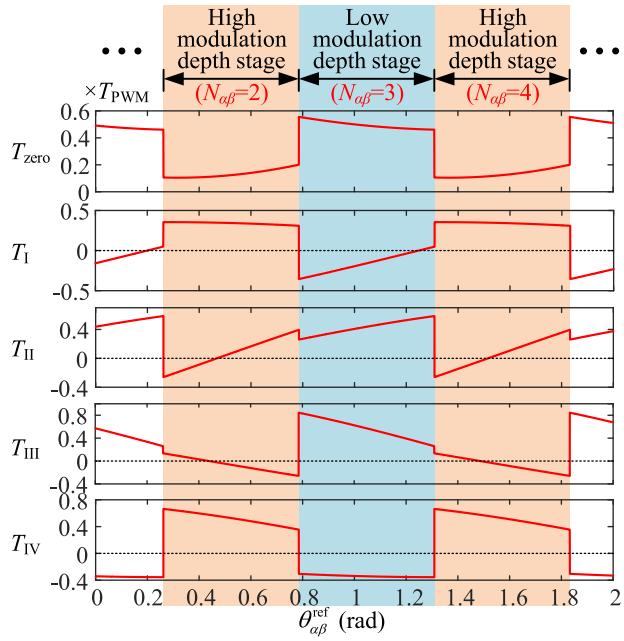

Fig. 7. T_{I}–T_{IV} and T_{zero} against $\theta_{\alpha\beta}^{\mathrm{ref}}$ under $\|\boldsymbol{u}_{\alpha\beta}^{\mathrm{ref}}\|=0.4U_{\mathrm{dc}}$, $\|\boldsymbol{u}_{xy}^{\mathrm{ref}}\|=0.15U_{\mathrm{dc}}$, and $\gamma=\pi/4$ after Step-1.

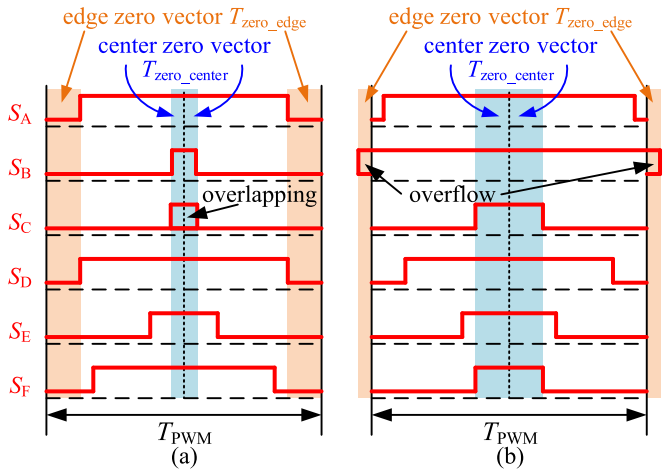

Fig. 8. Switching sequence of T_{A}–T_{F} under $\|\boldsymbol{u}_{\alpha\beta}^{\mathrm{ref}}\|=0.4U_{\mathrm{dc}}$, $\|\boldsymbol{u}_{xy}^{\mathrm{ref}}\|=0.15U_{\mathrm{dc}}$, and $\gamma=\pi/4$. (a) $\theta_{\alpha\beta}^{\mathrm{ref}}=0$. (b) $\theta_{\alpha\beta}^{\mathrm{ref}}=\pi/3$.

In conventional strategies, due to the non-negative T_{I}–T_{IV}, the above method for determining T_{A}–T_{F} can ensure equal dwell time of center zero vector ($T_{\mathrm{zero\_center}}$) and edge zero vector ($T_{\mathrm{zero\_edge}}$). However, since T_{I}–T_{IV} may be negative after Step-1 of the proposed design, it will lead to unequal $T_{\mathrm{zero\_center}}$ and $T_{\mathrm{zero\_edge}}$. As a more detailed explanation, based on the same conditions as Fig. 7(i.e., $\|\boldsymbol{u}_{\alpha\beta}^{\mathrm{ref}}\|=0.4U_{\mathrm{dc}}$, $\|\boldsymbol{u}_{xy}^{\mathrm{ref}}\|=0.15U_{\mathrm{dc}}$, $\gamma=\pi/4$), Fig. 8(a) and (b) shows the switching sequence of T_{A}–T_{F} obtained by (9) when $\theta_{\alpha\beta}^{\mathrm{ref}}=0$ and $\theta_{\alpha\beta}^{\mathrm{ref}}=\pi/3$, respectively. As can be seen, in Fig. 8(a), since the rising edge of S_{C} lags behind its falling edge, it results in positive $T_{\mathrm{zero\_edge}}$ but negative $T_{\mathrm{zero\_center}}$. On the other hand, in Fig. 8(b), since the high-level duration of S_{B} exceeding T_{PWM}, it results in positive $T_{\mathrm{zero\_center}}$

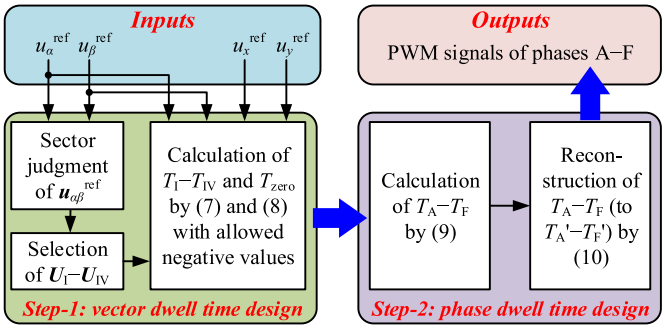

Fig. 9. Flowchart of the proposed SVPWM strategy.

but negative $T_{\text{zero\_edge}}$. In both cases, due to the inability to ensure that the dwell time of all phases is within [0, T_{PWM}], the corresponding switching sequences cannot be achieved in practice. In other words, at relatively high modulation depths, even if T_{zero} ($= T_{\text{zero\_center}}+T_{\text{zero\_edge}}$) can be always positive, modulation failure may still occur due to negative $T_{\text{zero\_center}}$ or negative $T_{\text{zero\_edge}}$.

Fortunately, as long as T_{zero} ($= T_{\text{zero\_center}}+T_{\text{zero\_edge}}$) is non-negative, such modulation failure can be avoided by further optimizing $T_{\text{zero\_center}}$ and $T_{\text{zero\_edge}}$. Specifically, if $T_{\text{zero}}\geq 0$, one can set $T_{\text{zero\_center}} = T_{\text{zero\_edge}} = 0.5T_{\text{zero}}\geq 0$ to ensure the dwell time of each phase is in an achievable state. To realize this, the dwell times of phases A–F should be adjusted accordingly. In detail, the dwell times T_A'–T_F' of each phase adjusted by this step can be obtained through (10) to realize $T_{\text{zero\_center}} = T_{\text{zero\_edge}}$

$$\begin{cases} T_j' = T_j + (T_{\text{PWM}} - \max\{T_A, T_B, T_C\} \\ \qquad - \min\{T_A, T_B, T_C\})/2 \\ T_k' = T_k + (T_{\text{PWM}} - \max\{T_D, T_E, T_F\} \\ \qquad - \min\{T_D, T_E, T_F\})/2 \end{cases} \tag{10}$$

where $j =$ A, B, C, and $k =$ D, E, F.

Finally, Fig. 9 displays the complete flowchart of the proposed SVPWM strategy.

C. Linear Modulation Boundary of the Proposed SVPWM Strategy

This section conducts an analytic analysis for the linear modulation boundary of the proposed SVPWM strategy under power sharing. As $\boldsymbol{u}_{\alpha\beta}^{\text{ref}}$ and $\boldsymbol{u}_{xy}^{\text{ref}}$ are both nonzero vectors under power sharing, two modulation indices $M_{\alpha\beta}$ and M_{xy} can be introduced to reflect the modulation depth of $\alpha\beta$ subspace and xy subspace, respectively. Their definitions are as follows:

$$M_{\alpha\beta} = \frac{\left\|\boldsymbol{u}_{\alpha\beta}^{\text{ref}}\right\|}{U_{\text{dc}}/2}, \quad M_{xy} = \frac{\left\|\boldsymbol{u}_{xy}^{\text{ref}}\right\|}{U_{\text{dc}}/2}. \tag{11}$$

According to the aforesaid design procedure, it can be known from Fig. 8 that non-negative $T_{\text{zero\_center}}$ and $T_{\text{zero\_edge}}$ are the preconditions for achieving linear modulation. Therefore, on the basis of (10), the linear modulation boundary of the proposed strategy corresponds to the case where the minimum value of T_{zero} is equal to 0.

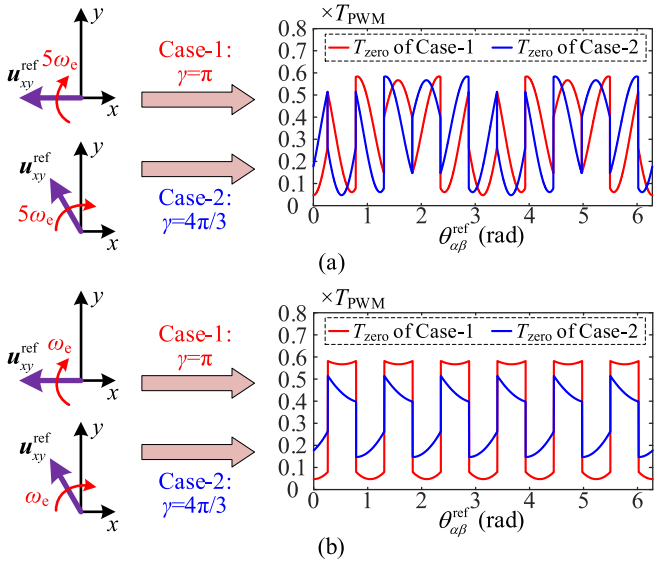

Fig. 10. Variations of T_{zero} under constant $\|\boldsymbol{u}_{\alpha\beta}^{\text{ref}}\|$ and $\|\boldsymbol{u}_{xy}^{\text{ref}}\|$ ($\|\boldsymbol{u}_{\alpha\beta}^{\text{ref}}\| = 0.4U_{\text{dc}}$, $\|\boldsymbol{u}_{xy}^{\text{ref}}\| = 0.15U_{\text{dc}}$). (a) $\boldsymbol{u}_{xy}^{\text{ref}}$ rotates with $5\omega_e$. (b) $\boldsymbol{u}_{xy}^{\text{ref}}$ rotates with ω_e.

For solving linear modulation boundary, the general approach is based on $\|\boldsymbol{u}_{\alpha\beta}^{\text{ref}}\|$ and $\|\boldsymbol{u}_{xy}^{\text{ref}}\|$, ensuring that the global minimum value of T_{zero} is equal to 0 when $\theta_{\alpha\beta}^{\text{ref}}$ and θ_{xy}^{ref} both vary from 0 to 2π. Essentially, such method only considers the amplitude relationship between $\boldsymbol{u}_{\alpha\beta}^{\text{ref}}$ and $\boldsymbol{u}_{xy}^{\text{ref}}$. In fact, however, without considering the factors such as the frequency relationship between $\boldsymbol{u}_{\alpha\beta}^{\text{ref}}$ and$\boldsymbol{u}_{xy}^{\text{ref}}$, it may not obtain the most accurate results.

For a more detailed explanation, Fig. 10 shows the effect of $\boldsymbol{u}_{xy}^{\text{ref}}$ rotation frequency on T_{zero} under constant $\|\boldsymbol{u}_{\alpha\beta}^{\text{ref}}\|$ and $\|\boldsymbol{u}_{xy}^{\text{ref}}\|$ ($\|\boldsymbol{u}_{\alpha\beta}^{\text{ref}}\| = 0.4U_{\text{dc}}$, $\|\boldsymbol{u}_{xy}^{\text{ref}}\| = 0.15U_{\text{dc}}$). First, Fig. 10(a) shows the T_{zero} when $\boldsymbol{u}_{xy}^{\text{ref}}$ rotates with $5\omega_e$ under two different phase angles γ. As seen, the influence of different γ on the minimum value of T_{zero} is negligible. Next, Fig. 10(b) shows the T_{zero} when $\boldsymbol{u}_{xy}^{\text{ref}}$ rotates with the fundamental frequency ω_e under the above γ angles. Compared with those in Fig. 10(a), it can be seen that the minimum value of T_{zero} is now changed with γ significantly. This means that even if $\|\boldsymbol{u}_{\alpha\beta}^{\text{ref}}\|$ and $\|\boldsymbol{u}_{xy}^{\text{ref}}\|$ remain constant, the lower the RVV rotational frequency, the more diverse the linear modulation capability may be.

Hence, to more accurately find the linear modulation boundary, it is vital to consider the frequency and phase relationship of each subspace RVV. With (5), (7), (8), and (11), the expression for T_{zero} considering all these factors can be derived as

$$T_{\text{zero}} = T_{\text{PWM}} \times \left[1 - \frac{\sqrt{3}}{2}\begin{pmatrix} M_{\alpha\beta}\cos[\theta_{\alpha\beta}^{\text{ref}} - (N_{\alpha\beta}-1)\frac{\pi}{6}] \\ -M_{xy}\cos[(\theta_{\alpha\beta}^{\text{ref}}+\gamma) + (N_{\alpha\beta}-1)\frac{5\pi}{6}]\end{pmatrix}\right]. \tag{12}$$

Equation (12) can be regarded as the analytical form of T_{zero} shown in Fig. 7. As intuitively seen from Fig. 7, T_{zero} is inconsistent between odd $N_{\alpha\beta}$ and even $N_{\alpha\beta}$. Fig. 11 illustrates the reason for such phenomenon. First, when $\boldsymbol{u}_{\alpha\beta}^{\text{ref}}$ is in the first sector of $\alpha\beta$ subspace ($N_{\alpha\beta} = 1$), Fig. 11(a) shows the distribution

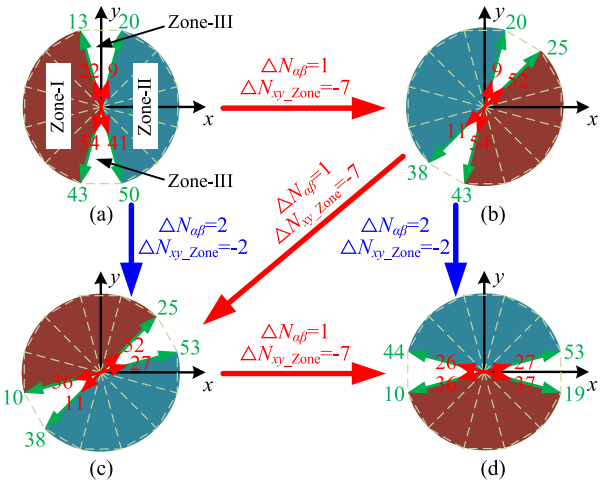

Fig. 11. Distribution of different zones in xy subspace when $\boldsymbol{u}_{\alpha\beta}^{\text{ref}}$ is in different sectors ($N_{\alpha\beta}$) of $\alpha\beta$ subspace. (a) $N_{\alpha\beta}=1$. (b) $N_{\alpha\beta}=2$. (c) $N_{\alpha\beta}=3$. (d) $N_{\alpha\beta}=4$.

of the eight candidate active vectors of the proposed SVPWM strategy in xy subspace. Taking these vectors as boundaries, the xy subspace can be divided into three zones, namely Zone-I (brown), Zone-II (blue), and Zone-III (white). Followed by the same principle, when $N_{\alpha\beta}$ is equal to 2, 3, and 4, distribution of the corresponding three zones in xy subspace can be obtained, as shown in Fig. 11(b), (c), and (d), respectively. As can be seen from Fig. 11(a)–(d), as long as $N_{\alpha\beta}$ increases by 1 ($\triangle N_{\alpha\beta}=1$), the sectors of Zone-I, Zone-II, and Zone-III in xy subspace all decrease by 7 ($\triangle N_{xy\_\text{Zone}}=-7$). However, when $N_{\alpha\beta}$ increases by 2 ($\triangle N_{\alpha\beta}=2$), $\triangle N_{xy\_\text{Zone}}$ becomes to -2.

The reason for dividing such zones in xy subspace based on the candidate vectors is that different zones use different types of vectors for synthesis, thereby leading to different modulation depths. As analyzed in Fig. 3, $\boldsymbol{u}_{\alpha\beta}^{\text{ref}}$ and $\boldsymbol{u}_{xy}^{\text{ref}}$ have the same rotation frequency, but their rotation direction is opposite. Thus, under any $N_{\alpha\beta}$, only $\triangle N_{xy\_\text{Zone}}=-\triangle N_{\alpha\beta}$ can ensure that the types of vectors for xy subspace synthesis remain unchanged. The $\triangle N_{xy\_\text{Zone}}=-2$ obtained from Fig. 11 for $\triangle N_{\alpha\beta}=2$ satisfies this condition, but $\triangle N_{xy\_\text{Zone}}=-7$ for $\triangle N_{\alpha\beta}=1$ obviously does not. So, it means that there are two kinds of modulation depths in xy subspace, reflected, respectively, when $N_{\alpha\beta}$ is odd and even. And it is also the reason why the dwell time of each vector shown in Fig. 7 cannot vary periodically in each $N_{\alpha\beta}$ sector. Due to this unique feature, to calculate the linear modulation boundary, it is necessary to judge the $N_{\alpha\beta}$ (odd or even) of $\boldsymbol{u}_{\alpha\beta}^{\text{ref}}$ when $\boldsymbol{u}_{xy}^{\text{ref}}$ is located in the zone with higher modulation depth. Such task depends on the position relationship between $\boldsymbol{u}_{\alpha\beta}^{\text{ref}}$and $\boldsymbol{u}_{xy}^{\text{ref}}$, which can be reflected by the phase angle γ. Thus, when $\boldsymbol{u}_{xy}^{\text{ref}}$ is located in the zone with higher modulation depth, the type of $N_{\alpha\beta}$ (odd or even) can be evaluated by γ, and the final conclusion can be provided as

$$\begin{cases}\text{if } \gamma\in[\frac{\pi}{2},\frac{3\pi}{2}), & \text{then } N_{\alpha\beta}=\text{odd}\\ \text{if } \gamma\in[0,\frac{\pi}{2})\cup[\frac{3\pi}{2},2\pi), & \text{then } N_{\alpha\beta}=\text{even}.\end{cases}\tag{13}$$

TABLE I
LINEAR MODULATION BOUNDARY OF THE PROPOSED SVPWM STRATEGY

Angle ranges of γ	Boundary curves of linear modulation
$\gamma=0$ or π	$M_{\alpha\beta}+M_{xy}-2/\sqrt{3}=0$
$\gamma\in(0,\frac{\pi}{2})\cup(\pi,\frac{3\pi}{2})$	$\begin{cases}f(M_{\alpha\beta},M_{xy},\gamma)-2/\sqrt{3}=0, & M_{\alpha\beta}<M_{xy}\\ f(M_{\alpha\beta},M_{xy},\gamma)+2/\sqrt{3}=0, & M_{\alpha\beta}>M_{xy}\\ M_{\alpha\beta}=M_{xy}=1/(\sqrt{3}\sin Z), & M_{\alpha\beta}=M_{xy}\end{cases}$
$\gamma\in[\frac{\pi}{2},\pi)$	$\begin{cases}f(M_{\alpha\beta},M_{xy},\gamma)+2/\sqrt{3}=0, & M_{\alpha\beta}<M_{xy}\\ f(M_{\alpha\beta},M_{xy},\gamma)-2/\sqrt{3}=0, & M_{\alpha\beta}>M_{xy}\\ M_{\alpha\beta}=M_{xy}=1/(\sqrt{3}\sin Z), & M_{\alpha\beta}=M_{xy}\end{cases}$
$\gamma\in[\frac{3\pi}{2},2\pi)$	$\begin{cases}f(M_{\alpha\beta},M_{xy},\gamma)-2/\sqrt{3}=0, & M_{\alpha\beta}<M_{xy}\\ f(M_{\alpha\beta},M_{xy},\gamma)+2/\sqrt{3}=0, & M_{\alpha\beta}>M_{xy}\\ M_{\alpha\beta}=M_{xy}=-1/(\sqrt{3}\sin Z), & M_{\alpha\beta}=M_{xy}\end{cases}$

By relying on the periodicity in each odd $N_{\alpha\beta}$ sectors and the periodicity in each even $N_{\alpha\beta}$ sectors, one can only analyze $N_{\alpha\beta}=1$ and $N_{\alpha\beta}=2$ for simplicity. Therefore, by combining (12), (13) and letting the minimum value of T_{zero} equal to 0, the linear modulation boundary of the proposed SVPWM strategy can be obtained based on the specific ranges of γ. The detailed results are listed in Table I. The function $f(M_{\alpha\beta}, M_{xy}, \gamma)$ is

$$\begin{aligned}&f(M_{\alpha\beta},M_{xy},\gamma)\\&\quad=M_{\alpha\beta}\cos\left[Z+\arctan\left(\frac{M_{\alpha\beta}+M_{xy}}{M_{xy}-M_{\alpha\beta}}\tan Z\right)\right]\\&\qquad-M_{xy}\cos\left[Z-\arctan\left(\frac{M_{\alpha\beta}+M_{xy}}{M_{xy}-M_{\alpha\beta}}\tan Z\right)\right]\end{aligned}\tag{14}$$

where $Z=\gamma/2+(N_{\alpha\beta}\text{-}1)\cdot\pi/2$; and $N_{\alpha\beta}$ (= 1 or 2) can be determined by (13) according to the specific angle of γ.

Based on (14) and Table I, Fig. 12(a) exhibits the linear modulation boundary of the proposed SVPWM strategy with γ ranging from 0 to 2π. Besides, Fig. 12(a) also shows the linear modulation boundary obtained without considering the frequency feature of the RVV. As a partial view, the two-dimensional cross-sectional images by Fig. 12(a) at $\gamma=\pi/4$ and $\gamma=\pi/2$ are shown in Fig. 12(b) and (c), respectively. From Fig. 12(a)–(c), three conclusions can be drawn as follows.

1) For power sharing scenarios, due to the reduced frequency of the RVV in xy subspace (fundamental frequency) compared with harmonic regulation scenarios, considering the RVV frequency feature can effectively excavate more regions where the proposed strategy can achieve linear modulation.
2) After considering the RVV frequency feature, different γ angles result in different degrees of linear modulation range expansion, but the most obvious expansion regions are all around $M_{\alpha\beta}=M_{xy}$.
3) The maximum achievable linear modulation range of the proposed SVPWM strategy corresponds to $\gamma=\pi/2$ or $3\pi/2$.

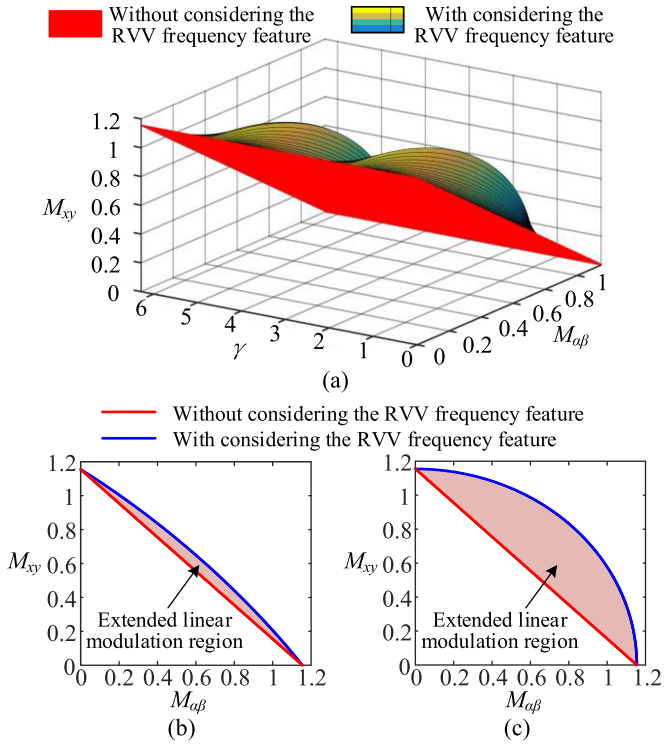

Fig. 12. Linear modulation boundary of the proposed SVPWM strategy. (a) Overall perspective. (b) Cross section at $\gamma = \pi/4$. (c) Cross section at $\gamma = \pi/2$.

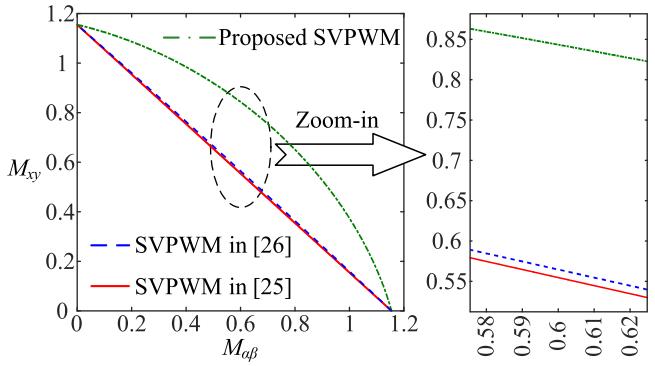

Fig. 13. Linear modulation boundary comparison of different VSD-based SVPWM strategies under power sharing when $\gamma = 5\pi/12$.

D. Comparisons With Other VSD-Based SVPWM Solutions

In this section, the basic VSD-4V SVPWM strategies and the two-modulation-stage-based SVPWM strategies presented in [25] and [26] are considered for comparisons.

1) Comparison of Linear Modulation Range: As a fair premise, the RVVs in $\alpha\beta$ and xy subspaces for all compared strategies are considered to rotate at a constant speed along a circular trajectory, so as to achieve circular rotational MMF [i.e., the RVVs in $\alpha\beta$ and xy subspaces should have the characteristics in Fig. 3 and (5)].

For the basic VSD-4V SVPWM strategies in [13], [15], [16], and [17], due to the constraints of non-negative dwell time of the basic vectors, all of them suffer from zero linear modulation range if the RVV amplitude in xy subspace is nonzero. For the strategy in [25], due to the split of modulation in $\alpha\beta$ subspace and xy subspace, its linear modulation boundary is determined by the non-negative T_{zero} in each modulation stage, and the final result can be given as

$$M_{\alpha\beta} + M_{xy} - 2/\sqrt{3} = 0. \tag{15}$$

Different from [25], [26] considers T_{zero} from the complete PWM cycle. This will slightly help to extend the linear modulation range, because it is only necessary to ensure non-negative T_{zero} in the whole PWM cycle (no need to further ensure that T_{zero} of each modulation stage is non-negative). By means of the analysis method in Section III-C, the linear modulation boundary of the SVPWM strategy in [26] under power sharing can be derived as

$$M_{\alpha\beta}\cos\left[Y + \arctan\left(\frac{M_{xy} - M_{\alpha\beta}}{M_{\alpha\beta} + M_{xy}}\tan Y\right)\right] + M_{xy}\cos\left[Y - \arctan\left(\frac{M_{xy} - M_{\alpha\beta}}{M_{\alpha\beta} + M_{xy}}\tan Y\right)\right] + \frac{2}{\sqrt{3}} = 0 \tag{16}$$

where $Y = \gamma/2 + \text{floor}(12.5 - 6\gamma/\pi)\cdot\pi/12$. From (16), it can be further proven that the maximum linear modulation boundary corresponds to $\gamma = \pi/12 + k\cdot\pi/6$, where $k = 0, 1, \ldots, 11$.

Based on Table I and (14)–(16), Fig. 13 graphically compares the linear modulation boundaries of different SVPWM strategies. γ is chosen to be $5\pi/12$. As seen, even though $\gamma = 5\pi/12$ corresponds to the maximum linear modulation capability of the strategy in [26], the linear modulation range only slightly improves compared with that in [25]. For the proposed strategy, although $\gamma = 5\pi/12$ does not correspond to its maximum linear modulation capability, the improvement over the strategies in [25] and [26] is still prominent.

On the other hand, if M_{xy} in (14)–(16) are all equal to 0 (i.e., balanced power sharing), then all strategies will have the same linear modulation boundary as follows:

$$M_{\alpha\beta} = 2/\sqrt{3}, \quad M_{xy} = 0. \tag{17}$$

2) Comparison of Computational Burden: For the basic VSD-4V strategies, the four active vectors depend entirely on $\boldsymbol{u}_{\alpha\beta}^{\text{ref}}$, so sector judgment only needs to be performed in $\alpha\beta$ subspace. Then, based on five calculations of vector dwell time (four active vectors plus 1 zero vector) and six calculations of dwell time for each phase A–F, the operation task is completed.

For the strategies in [25] and [26], the doubled modulation stages mean almost all operations of the basic VSD-4V strategies need to be doubled. The only difference is that T_{zero} only needs to be calculated once in [26], while it requires twice in [25] due to the split PWM cycle.

For the proposed strategy, even if there are a total of eight candidate vectors (four original vectors and four nonoriginal vectors) in a modulation cycle, the four nonoriginal vectors are equivalent vectors under negative dwell time of the four original vectors. Thus, as long as four original vectors are selected

TABLE II
PERFORMANCE COMPARISON OF DIFFERENT VSD-BASED SVPWM STRATEGIES

SVPWM strategies	Performance indicators					
	Linear modulation range		Computational burden (in one PWM cycle)			
	For balanced power sharing	For unbalanced power sharing	Number of sector judgments	Number of calculations for vector dwell time	Number of calculations for phase dwell time	Other additional operations
Basic VSD-4V strategies in [13], [15], [16], [17]	$M_{\alpha\beta}$≤2/sqrt(3), M_{xy}=0	Zero	1	5	6	No
Two-modulation-stage-based strategy in [25]	$M_{\alpha\beta}$≤2/sqrt(3), M_{xy}=0	Medium	2	10	12	Split the PWM cycle by $\|\|\boldsymbol{u}_{\alpha\beta}^{\mathrm{ref}}\|\|$ and $\|\|\boldsymbol{u}_{xy}^{\mathrm{ref}}\|\|$
Two-modulation-stage-based strategy in [26]	$M_{\alpha\beta}$≤2/sqrt(3), M_{xy}=0	Slightly larger than medium	2	9	12	No
Proposed strategy	$M_{\alpha\beta}$≤2/sqrt(3), M_{xy}=0	Maximum	1	5	6	Average $T_{\mathrm{zero\_center}}$ and $T_{\mathrm{zero\_edge}}$

through the sector judgment on $\boldsymbol{u}_{\alpha\beta}^{\mathrm{ref}}$, then which of the eight candidate vectors should be finally used depends entirely on the positive or negative values of the dwell time calculation results of the four original vectors [as can be seen from (7) and (8), positive or negative only depends on $N_{\alpha\beta}$ and the given $u_{\alpha}^{\mathrm{ref}}$, u_{β}^{ref}, u_{x}^{ref}, and u_{y}^{ref}]. In other words, sector judgment only needs to be performed once for $N_{\alpha\beta}$, while the calculation of vector dwell time only needs to be focused on the four original active vectors and one zero vector (i.e., a total of five calculations). Moreover, from Fig. 9, it can be seen that except the need of (10) to average $T_{\mathrm{zero\_center}}$ and $T_{\mathrm{zero\_edge}}$, the number of calculations for phase dwell time is also kept at the minimum value of six for the six-phase machine.

3) Summary: Different features of all the relevant SVPWM strategies are summarized in Table II. Among different strategies, the proposed strategy has the maximum linear modulation range under unbalanced power sharing. Besides, in terms of computational burden, compared with the strategies in [25] and [26] that also have linear modulation capability under unbalanced power sharing, the proposed strategy has fewer sector judgments, fewer calculations for vector dwell time, and fewer calculations for phase dwell time, which can compensate for the need to average $T_{\mathrm{zero\_center}}$ and $T_{\mathrm{zero\_edge}}$. In conclusion, the proposed SVPWM strategy can be considered as a competitive solution for DTP machine drives under power sharing conditions.

IV. EXPERIMENTAL VERIFICATION

In machine control framework, the factor directly related to SVPWM is the voltage commands. Hence, to more clearly and intuitively verify the principle of the proposed strategy and compare it with other strategies under power sharing, the experiment with open-loop voltage direct control is first conducted. After that, the power sharing results of the proposed SVPWM strategy under complete closed-loop control are further presented.

By taking DTP permanent-magnet (PM) synchronous machine (PMSM) as the tested machine, Fig. 14 shows the overall experimental setup. The specific parameters of the DTP PMSM drives are listed in Table III.

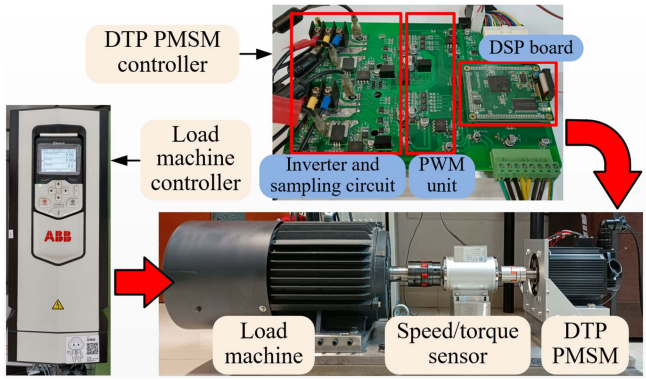

Fig. 14. Experimental setup of the DTP PMSM drives.

TABLE III
PARAMETERS OF THE DTP PMSM DRIVES IN THE EXPERIMENT

Parameters	Symbols	Values
Rated speed	n_{N}	1000 r/min
Rated torque	T_{N}	9.55 N·m
Rated stator RMS current	i_{N}	7 A
Pole pair number	n_{p}	5
Stator resistance	R_{s}	0.6 Ω
dq-axis inductance	L_d, L_q	8 mH
PM flux linkage	ψ_{f}	0.08 Wb
Moment of inertia	J	0.0017 kg·m^2
PWM cycle	T_{PWM}	100 μs

A. Open-Loop Voltage Control

In this experiment, the DTP PMSM is controlled by the diagram shown in Fig. 15 for open-loop power sharing. As analyzed in Section II-B, unbalanced power sharing state of the machine corresponds to nonzero $\boldsymbol{u}_{\alpha\beta}^{\mathrm{ref}}$ and $\boldsymbol{u}_{xy}^{\mathrm{ref}}$ both rotating at the fundamental frequency. Thus, open-loop power sharing can be achieved by setting reference voltages u_d^{ref}, u_q^{ref}, u_{z1}^{ref}, and u_{z2}^{ref} in synchronous frame to specific dc values directly. As long as u_{z1}^{ref} and u_{z2}^{ref} are not zero simultaneously, unbalanced power sharing can be then achieved. The inverse Park transformation from dq and $z1z2$ subspaces to $\alpha\beta$ and xy subspaces can be

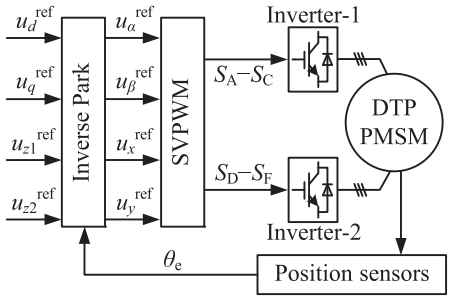

Fig. 15. Diagram of open-loop voltage control for power sharing.

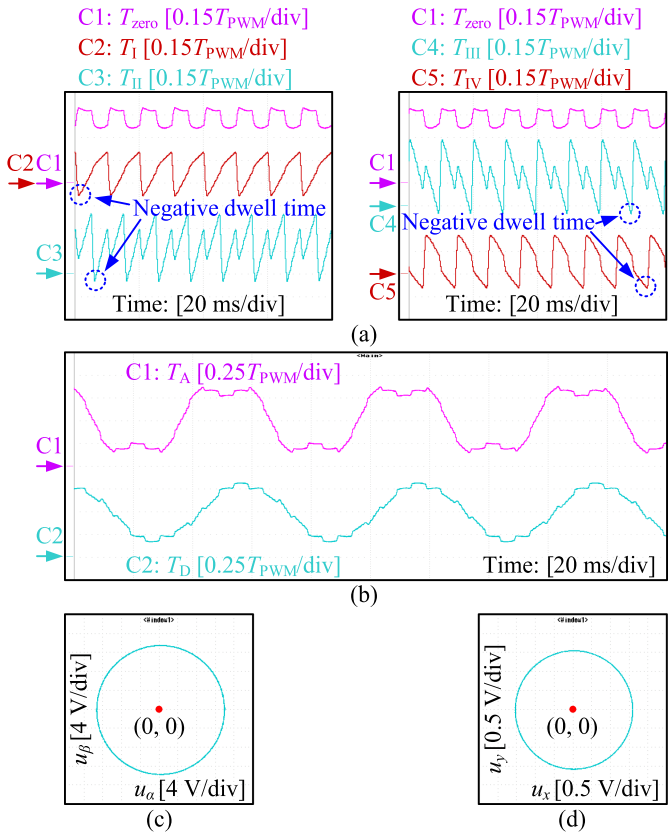

Fig. 16. Voltage control with u_d^{ref}= -4 V,u_q^{ref} = 13 V, u_{z1}^{ref}= −1.2 V, and u_{z2}^{ref}= −1 V for the proposed SVPWM strategy with Step-1 under $U_{\text{dc}} = 40$ V. (a) Dwell times of the basic vectors. (b) Phase dwell times T_{A} and T_{D}. (c) Actual voltage trajectory in $\alpha\beta$ subspace. (d) Actual voltage trajectory in xy subspace.

represented in complex vector form as [27]

$$\boldsymbol{F}_{\alpha\beta} = \boldsymbol{F}_{dq}\mathrm{e}^{\mathrm{j}\theta_{\text{e}}}, \quad \boldsymbol{F}_{xy} = \boldsymbol{F}_{z1z2}\mathrm{e}^{-\mathrm{j}\theta_{\text{e}}} \tag{18}$$

where θ_{e} is the rotor electrical position of the DTP PMSM.

1) Verification of the Two-Step Design of the Proposed SVPWM Strategy: First, Fig. 16 shows the experimental results for the proposed SVPWM strategy with only Step-1. The reference voltages are selected as u_d^{ref}= −4 V, u_q^{ref}= 13 V, u_{z1}^{ref}= −1.2 V, and u_{z2}^{ref}= −1 V. The dc bus voltage U_{dc} is 40 V. The load torque provided by the load machine is adjusted to make the speed equal to

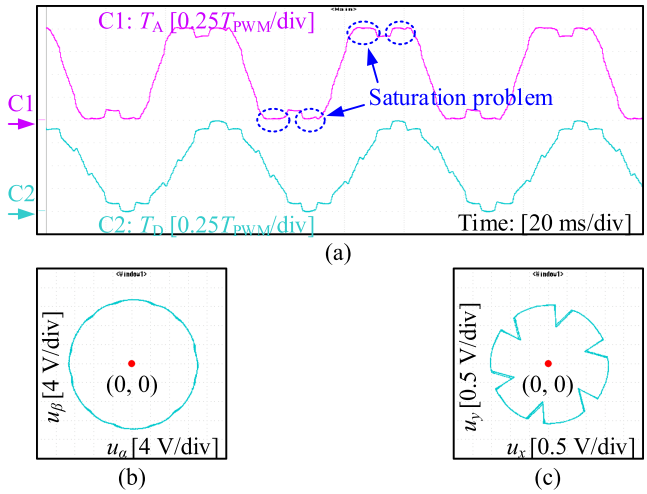

Fig. 17. Voltage control with u_d^{ref}= −4 V, u_q^{ref}= 13 V, u_{z1}^{ref}= −1.2 V, and u_{z2}^{ref}= −1 V for the proposed SVPWM strategy with Step-1 under $U_{\text{dc}} = 26$ V. (a) Phase dwell times T_{A} and T_{D}. (b) Actual voltage trajectory in $\alpha\beta$ subspace. (c) Actual voltage trajectory in xy subspace.

200 r/min. As can be seen by Fig. 16(a), with Step-1, negative dwell times of active vectors occur sometimes to provide preconditions for synthesizing the non-zero $\boldsymbol{u}_{\alpha\beta}^{\text{ref}}$ and $\boldsymbol{u}_{xy}^{\text{ref}}$. Besides, Fig. 16(b) shows the phase dwell times T_{A} and T_{D} (respectively, represents the dwell time of the two subthree-phase winding sets). Due to the relatively low modulation depth in this case, T_{A} and T_{D} obtained by (9) [i.e., without the optimization of (10) by Step-2] can be within the range of [0, T_{PWM}]. Hence, linear modulation in both $\alpha\beta$ and xy subspaces can be achieved, and the actual voltage trajectories in $\alpha\beta$ and xy subspaces are both circular with no distortion, as shown in Fig. 16(c) and (d), respectively.

Next, based on the same speed, u_d^{ref}, u_q^{ref}, u_{z1}^{ref}, and u_{z2}^{ref}, the experiment for the proposed SVPWM strategy with only Step-1 is further conducted by reducing U_{dc} to 26 V. In this case, it can be observed from Fig. 17(a) that T_{A} has reached the saturation state (0 and T_{PWM}) for a certain time. Consequently, overmodulation occurs and the actual voltage trajectories in $\alpha\beta$ and xy subspaces depicted in Fig. 17(b) and (c) no longer appear to be circular, especially that in xy subspace.

Then, with U_{dc} = 26 V and the same speed, u_d^{ref}, u_q^{ref}, u_{z1}^{ref}, and u_{z2}^{ref}, Fig. 18 shows the experimental results for the proposed SVPWM strategy with Step-1 and Step-2. Compared with Fig. 17(a), it can be observed by Fig. 18(a) that the waveform shape of phase dwell time has been modified through Step-2. Since T_{A}' is no longer maintained at 0 and T_{PWM} for a certain time, the saturation state is exited. Hence, both $\alpha\beta$ subspace and xy subspace achieve linear modulation again, resulting in the circular actual voltage trajectories shown in Fig. 18(b) and (c), respectively. Compared with the experimental results in Fig. 17, the function of Step-2 to further expand the linear modulation range can be, therefore, confirmed.

Moreover, by the experimental results in Fig. 18, one can also find that the linear modulation boundary of the proposed SVPWM strategy is just reached. This is because the minimum

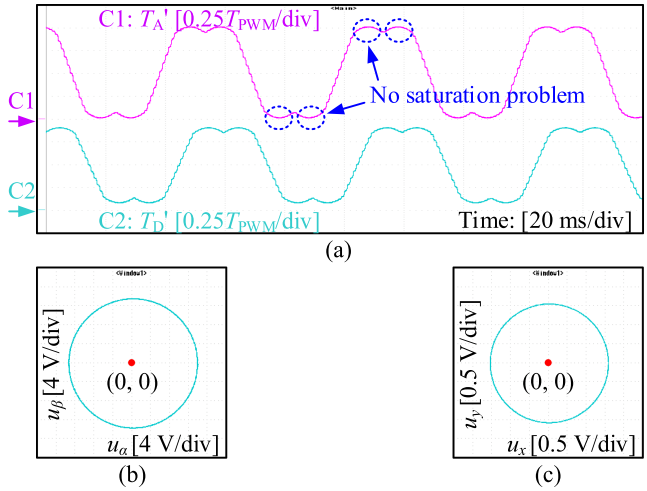

Fig. 18. Voltage control with $u_d^{\text{ref}} = -4$ V, $u_q^{\text{ref}} = 13$ V, $u_{z1}^{\text{ref}} = -1.2$ V, and $u_{z2}^{\text{ref}} = -1$ V for the proposed SVPWM strategy with Step-1 and Step-2 under $U_{\text{dc}} = 26$ V. (a) Phase dwell times T_A' and T_D'. (b) Actual voltage trajectory in $\alpha\beta$ subspace. (c) Actual voltage trajectory in xy subspace.

and maximum values of T_A' and T_D' happen to be 0 and T_{PWM}, respectively, while the actual voltage trajectories in both subspaces are still circular. In this case, based on the specific u_d^{ref}, u_q^{ref}, u_{z1}^{ref}, u_{z2}^{ref}, and U_{dc} given previously, it can be calculated by (11), (18), and Fig. 3 that

$$\begin{cases} M_{\alpha\beta} = \dfrac{\sqrt{{u_d^{\text{ref}}}^2 + {u_q^{\text{ref}}}^2}}{U_{\text{dc}}/2} = 1.0463 \\ M_{xy} = \dfrac{\sqrt{{u_{z1}^{\text{ref}}}^2 + {u_{z2}^{\text{ref}}}^2}}{U_{\text{dc}}/2} = 0.1202 \\ \gamma = \arctan\left(\dfrac{u_{z1}^{\text{ref}}}{u_{z2}^{\text{ref}}}\right) - \arctan\left(-\dfrac{u_d^{\text{ref}}}{u_q^{\text{ref}}}\right) = 0.5776 \text{ rad}. \end{cases} \tag{19}$$

Since the resulted $M_{\alpha\beta}$, M_{xy}, and γ generally meet the relationship in Table I, the correctness of theoretical analysis regarding linear modulation boundary of the proposed SVPWM strategy can be verified.

2) Linear Modulation Range Comparison of Different SVPWM Strategies: This experiment compares the linear modulation range of different SVPWM strategies when the DTP PMSM is under power sharing. In addition to the proposed strategy, the basic VSD-4V SVPWM strategy in [15] (Strategy-1) and the two-modulation-stage-based SVPWM strategy in [26] (Strategy-2) are considered. Same working conditions for all the three strategies are guaranteed by the same U_{dc} and the same reference voltages ($u_d^{\text{ref}} = -1.4$ V, $u_q^{\text{ref}} = 12$ V, $u_{z1}^{\text{ref}} = -1.7$ V, and $u_{z2}^{\text{ref}} = -0.24$ V). The speed of the DTP PMSM is maintained at 150 r/min in all comparisons by adjusting the load torque provided by the load machine.

First, the comparison is carried out under $U_{\text{dc}} = 28$ V. Fig. 19(a) shows the actual voltage trajectory and boundary of the effective modulation range (BEMR) in $\alpha\beta$ subspace under the three strategies, while those in xy subspace under the three strategies are given in Fig. 19(b). The BEMRs in $\alpha\beta$ and xy subspaces are obtained by the maximum achievable $\|\boldsymbol{u}_{\alpha\beta}^{\text{ref}}\|$ and $\|\boldsymbol{u}_{xy}^{\text{ref}}\|$ without changing $\|\boldsymbol{u}_{\alpha\beta}^{\text{ref}}\|/\|\boldsymbol{u}_{xy}^{\text{ref}}\|$, and the maximum achievable $\|\boldsymbol{u}_{\alpha\beta}^{\text{ref}}\|$ and $\|\boldsymbol{u}_{xy}^{\text{ref}}\|$ of Strategy-1, Strategy-2, and the proposed strategy are determined by the modulation constraints in [15] and [26], and this article, respectively. Since the RVVs in $\alpha\beta$ and xy subspaces of all the strategies rotate along circular trajectories, the linear modulation boundary of each strategy corresponds to the inscribed circle of its BEMRs.

From Fig. 19(a-1) and (b-1), it can be noticed that although there are certain regions within the BEMRs of Strategy-1, the inscribed circle radius of BEMR in both subspaces is 0. Thus, for such case with $\|\boldsymbol{u}_{\alpha\beta}^{\text{ref}}\| \neq 0$ and $\|\boldsymbol{u}_{xy}^{\text{ref}}\| \neq 0$, linear modulation in $\alpha\beta$ and xy subspaces cannot be achieved. For Strategy-2, it can be found from Fig. 19(a-2) and (b-2) that the inscribed circle radius $r_{\alpha\beta}$ of BEMR in $\alpha\beta$ subspace and the inscribed circle radius r_{xy} of BEMR in xy subspace are 14.20 V and 2.019 V, respectively. Since $r_{\alpha\beta} > \|\boldsymbol{u}_{\alpha\beta}^{\text{ref}}\| = 12.08$ V and $r_{xy} > \|\boldsymbol{u}_{xy}^{\text{ref}}\| = 1.717$ V, linear modulation in both subspaces is achieved. As a result, the actual voltage trajectories in $\alpha\beta$ and xy subspaces are both circular. For the proposed strategy, it can be seen from Fig. 19(a-3) and (b-3) that it not only has circular actual voltage trajectories in $\alpha\beta$ and xy subspaces, but also has higher $r_{\alpha\beta}$ (15.47 V) and higher r_{xy} (2.198 V), which means the extended linear modulation range can be possessed.

Next, the three strategies are retested under a reduced U_{dc} of 22 V. The experimental results under this condition are shown in Fig. 20. Due to the decrease in dc bus voltage, the BEMRs of each strategy shrink accordingly. For Strategy-1, since the inscribed circle radius of BEMR in both subspaces is still 0, the distorted modulation in $\alpha\beta$ and xy subspaces shown in Fig. 20(a-1) and (b-1) are similar to those in Fig. 19(a-1) and (b-1), respectively. Regarding Strategy-2, as seen by Fig. 20(a-2) and (b-2), $r_{\alpha\beta}$ and r_{xy} are reduced to 11.16 V and 1.586 V, respectively. Due to $r_{\alpha\beta} < \|\boldsymbol{u}_{\alpha\beta}^{\text{ref}}\|$ and $r_{xy} < \|\boldsymbol{u}_{xy}^{\text{ref}}\|$, the actual voltage trajectories in $\alpha\beta$ and xy subspaces completely coincide with the BEMR of the corresponding subspaces and, hence, overmodulation occurs. In this case, only the proposed strategy can maintain linear modulation in both subspaces. And this is because $r_{\alpha\beta}$ (12.15 V) and r_{xy} (1.727 V) are still not less than $\|\boldsymbol{u}_{\alpha\beta}^{\text{ref}}\|$ and $\|\boldsymbol{u}_{xy}^{\text{ref}}\|$, respectively, as shown in Fig. 20(a-3) and (b-3).

Furthermore, under the given reference voltages ($u_d^{\text{ref}} = -1.4$ V, $u_q^{\text{ref}} = 12$ V, $u_{z1}^{\text{ref}} = -1.7$ V, $u_{z2}^{\text{ref}} = -0.24$ V), by using (18) and VSD inverse transformation, the expected fundamental components of phase voltages u_A and u_D can be calculated as 12.6265 V and 11.7638 V, respectively. Fig. 20(d) and (e) shows the fast Fourier transform (FFT) results for the equivalent u_A and u_D, respectively, under the three strategies with $U_{\text{dc}} = 22$ V. Since the proposed strategy can synthesize circular rotating RVVs in both subspaces, not only the desired fundamental components of u_A and u_D are output, but also the total harmonic distortion (THD) values are the minimal. For Strategy-1, although the fundamental components of u_A and u_D are close to the expected values, the most obvious distorted modulation trajectories in $\alpha\beta$ and xy subspaces lead to the highest THD. For Strategy-2, although the distortion of the modulation trajectories in $\alpha\beta$ and xy subspaces is not significant, the actual trajectories have shrunk. Thus, in addition to the increase in THD of u_A and u_D compared with the proposed strategy, the main problem is also reflected in the decrease in fundamental output capability.

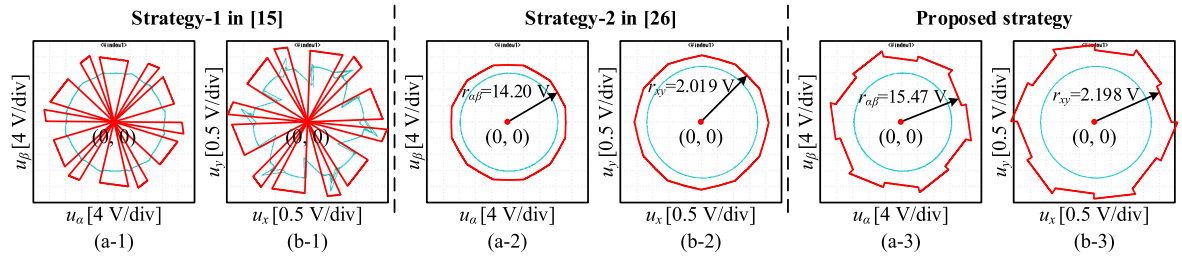

Fig. 19. Voltage control with $u_d^{\text{ref}} = -1.4$ V, $u_q^{\text{ref}} = 12$ V, $u_{z1}^{\text{ref}} = -1.7$ V, and $u_{z2}^{\text{ref}} = -0.24$ V under $U_{\text{dc}} = 28$ V using the SVPWM strategy in [15] (Strategy-1), the SVPWM strategy in [26] (Strategy-2), and the proposed SVPWM strategy. Actual voltage trajectory (cyan) and BEMR (red) under the three strategies in (a) $\alpha\beta$ subspace and (b) xy subspace.

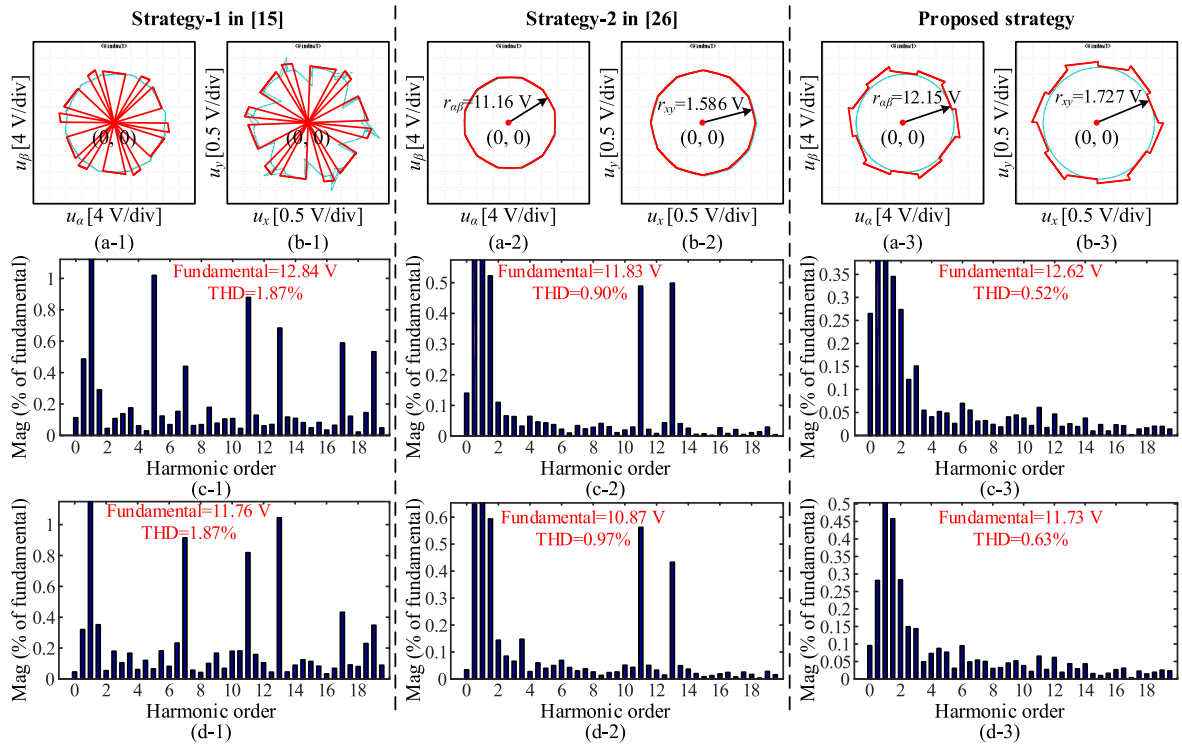

Fig. 20. Voltage control with $u_d^{\text{ref}} = -1.4$ V, $u_q^{\text{ref}} = 12$ V, $u_{z1}^{\text{ref}} = -1.7$ V, and $u_{z2}^{\text{ref}} = -0.24$ V under $U_{\text{dc}} = 22$ V using the SVPWM strategy in [15] (Strategy-1), the SVPWM strategy in [26] (Strategy-2), and the proposed SVPWM strategy. Actual voltage trajectory (cyan) and BEMR (red) under the three strategies in (a) $\alpha\beta$ subspace and (b) xy subspace. FFT results under the three strategies for the (c) equivalent u_{A} and (d) equivalent u_{D}.

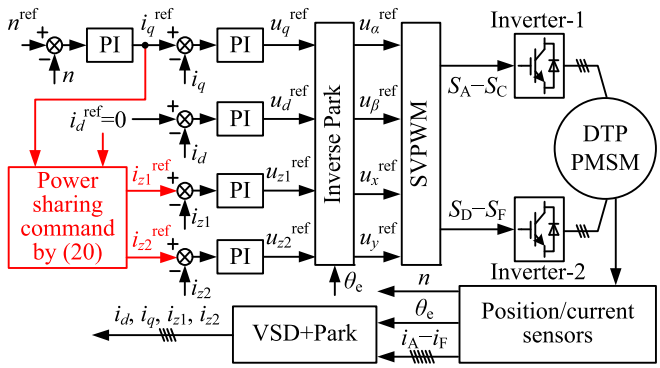

Fig. 21. Diagram of closed-loop control for power sharing.

3) Investigation of Computation Time for Different SVPWM Strategies: To further investigate the computational burden of different SVPWM strategies under experimental conditions, based on the control structure shown in Fig. 15 and the TI microcontroller TMS320F28379D, the measured results of computation time for each strategy within a modulation cycle are shown in Table IV. As seen, due to the doubled modulation stage, the strategies in [25] and [26] require more computation time than the basic VSD-4V strategy in [15]. Besides, the computation time of the strategy in [25] is higher than that in [26] due to one more calculation for vector dwell time and the additional operation to split the PWM cycle, as illustrated in Table II. For the proposed strategy, if only Step-1 is executed, it will have similar computational tasks to the basic VSD-4V strategy in

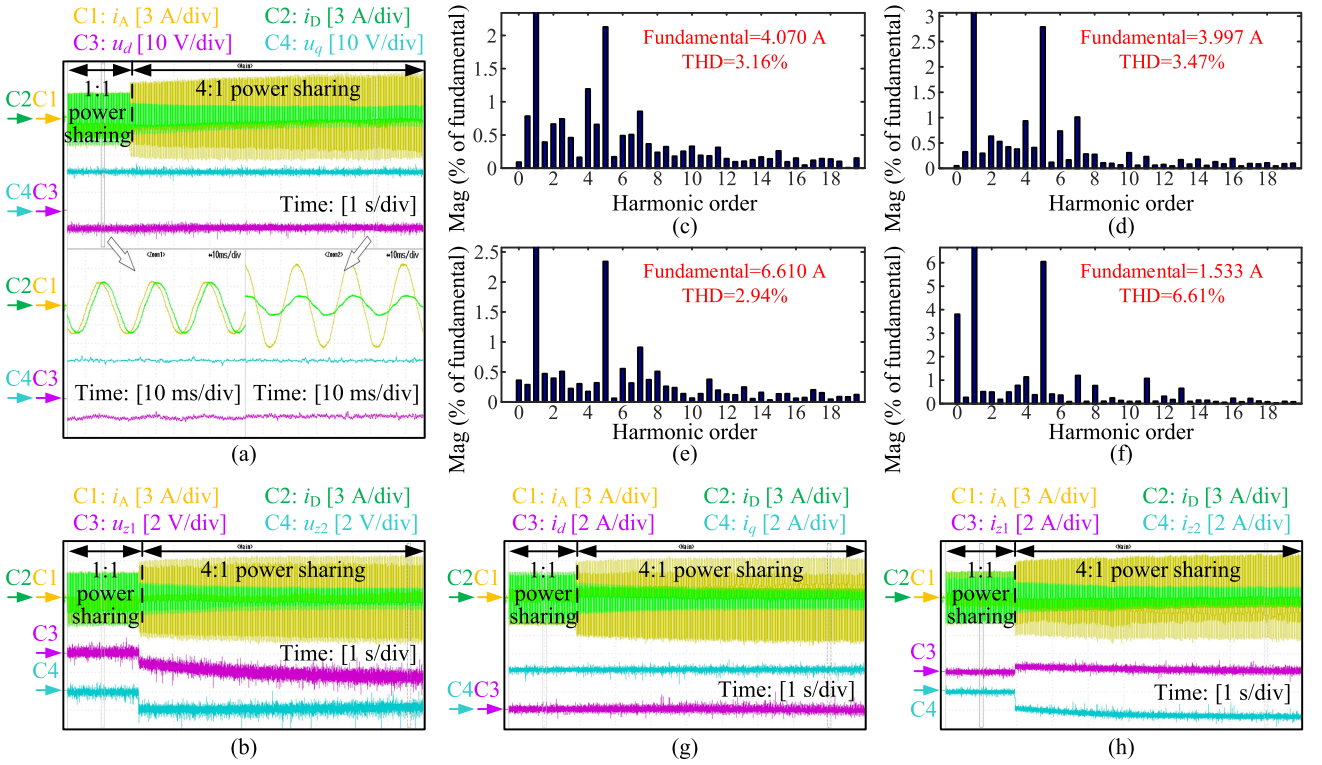

Fig. 22. Closed-loop control with $U_{dc} = 60$ V, reference speed = 400 r/min, load torque = 5 Nm, and power sharing ratio from 1:1 to 4:1 for the proposed SVPWM strategy. (a) i_A, i_D, u_d, and u_q. (b) i_A, i_D, u_{z1}, and u_{z2}. (c) FFT results for i_A under 1:1 power sharing. (d) FFT results for i_D under 1:1 power sharing. (e) FFT results for i_A under 4:1 power sharing. (f) FFT results for i_D under 4:1 power sharing. (g) i_A, i_D, i_d, and i_q. (h) i_A, i_D, i_{z1}, and i_{z2}.

TABLE IV
COMPUTATION TIMES OF DIFFERENT STRATEGIES IN THE EXPERIMENT

SVPWM strategies	Computation times (in one PWM cycle)
Basic VSD-4V strategy in [15]	41.27 μs
Two-modulation-stage-based strategy in [25]	62.03 μs
Two-modulation-stage-based strategy in [26]	49.29 μs
Proposed strategy with Step-1	41.15 μs
Proposed strategy with Step-1 and Step-2	51.86 μs

[15] (details are in Table II). And the experimental results in Table IV can also verify this. In addition, if both Step-1 and Step-2 of the proposed strategy are executed, the computation time is still lower than the strategy in [25] and almost the same as the strategy in [26]. This indicates that the two-stage modulation avoided by the proposed strategy can basically compensate for the additional computation time required to average $T_{\text{zero\_center}}$ and $T_{\text{zero\_edge}}$ in Step-2.

B. Closed-Loop Control

In this experiment, the proposed SVPWM strategy is investigated by closed-loop power sharing control. To achieve minimum copper loss, (3) should be satisfied. Optionally, based on (18), (3) can be realized by setting reference currents i_{z1}^{ref} and i_{z2}^{ref} in $z1z2$ synchronous frame as

$$i_{z1}^{\text{ref}} = (K_1 - K_2) i_d^{\text{ref}}, \quad i_{z2}^{\text{ref}} = (-K_1 + K_2) i_q^{\text{ref}}. \tag{20}$$

The control diagram is shown in Fig. 21. By setting U_{dc} to 60 V, reference speed n^{ref} to 400 r/min, and load torque to 5 Nm, Fig. 22 provides the dynamic results when power sharing command for the two subthree-phase winding sets changes from 1:1 to 4:1.

During the switching of power sharing ratio, Fig. 22(a) and (b), respectively, shows the changes in dq-axis voltages and $z1z2$-axis voltages with the changes in phase currents i_A and i_D. As seen, when power sharing ratio is 1:1, u_d, u_q, u_{z1}, and u_{z2} are -9 V, 21 V, 0 V, and 0 V, respectively, resulting in $\|\boldsymbol{u}_{\alpha\beta}^{\text{ref}}\| \neq 0$ and $\|\boldsymbol{u}_{xy}^{\text{ref}}\| = 0$. When power sharing ratio is switched to 4:1, u_d, u_q, u_{z1}, and u_{z2} are -9 V, 21 V, -2.4 V, and -1.8 V, respectively. Under 60 V dc bus voltage, similar to (19), one can calculate that $M_{\alpha\beta}$, M_{xy}, and γ here are 0.3808, 0.05, and 0.5224 rad, respectively. Based on these $M_{\alpha\beta}$, M_{xy}, and γ, it is known from (14) and Table I that the proposed SVPWM strategy can achieve linear modulation for 4:1 power sharing. Moreover, Fig. 22(c) and (d) shows the FFT results for i_A and i_D under 1:1 power sharing, respectively, while the corresponding results under 4:1 power sharing are given in Fig. 22(e) and (f). With the linear modulation, the main source of current THD is the nonideal characteristics such as inverter nonlinearity. The corresponding problem can be solved by further introducing the well-developed harmonic suppression strategies.

To further demonstrate the implementation principle of power sharing under current closed-loop control, Fig. 22(g) and (h), respectively, shows the changes in dq-axis currents and $z1z2$-axis currents with the changes in i_{A} and i_{D}. Similar to the dq-axis voltages shown in Fig. 22(a), the dq-axis currents shown in Fig. 22(g) also remain unchanged ($i_d = 0$ A and $i_q = 4.2$ A) before and after the power sharing ratio change, verifying that the dq-axis variables only reflect the total power and are independent of power imbalance. On the other hand, the $z1z2$-axis currents shown in Fig. 22(h) are both 0 A under 1:1 power sharing, while they are finally stabilized at 0 A and -2.6 A under 4:1 power sharing, respectively. Under 4:1 power sharing command (i.e., $K_1 = 0.8$, $K_2 = 0.2$), since $i_d = 0$ A, $i_q = 4.2$ A, $i_{z1} = 0$ A, and $i_{z2} = -2.6$ A are generally in accordance with (20), it means that the 4:1 power sharing is finally achieved by the closed-loop control.

V. Conclusion

This article proposes a new VSD-based SVPWM strategy for DTP machine drives under unbalanced power sharing conditions. According to the characteristics of the RVVs under power sharing, a two-step-based design procedure is illustrated to form the SVPWM strategy. The first step is to remove the non-negative dwell time constraints of the basic vectors. By this way, the achievable direction of nonzero vector synthesis becomes arbitrary, and the nonzero RVV linear modulation capability in both $\alpha\beta$ and xy subspaces can be created. Considering the unique dwell time features of the vectors resulting from the first step, the second step further extends the linear modulation range by averaging the dwell time of center zero vector and edge zero vector. For solving the linear modulation boundary in such case, an analysis method considering the RVV frequency feature is also presented. Compared with other typical VSD-based SVPWM strategies, the theoretical and experimental analyses indicate that the proposed strategy can be a competitive alternative for DTP machine drives with power sharing requirements due to the extended linear modulation range.

References

[1] S. Wang, K. Imai, and S. Doki, "A novel decoupling control scheme for non-salient multi-three-phase synchronous machines based on multi-stator model," *IEEE Trans. Ind. Appl.*, vol. 59, no. 1, pp. 886–896, Jan./Feb. 2023.

[2] S. Rubino, F. Mandrile, E. Armando, I. R. Bojoi, and L. Zarri, "Fault-tolerant torque controller based on adaptive decoupled multi-stator modeling for multi-three-phase induction motor drives," *IEEE Trans. Ind. Appl.*, vol. 58, no. 6, pp. 7318–7335, Nov./Dec. 2022.

[3] I. Subotic, O. Dordevic, J. B. Gomm, and E. Levi, "Active and reactive power sharing between three-phase winding sets of a multiphase induction machine," *IEEE Trans. Energy Convers.*, vol. 34, no. 3, pp. 1401–1410, Sep. 2019.

[4] S.-W. Hwang, D.-K. Son, S.-H. Park, G.-H. Lee, Y.-D. Yoon, and M.-S. Lim, "Design and analysis of dual stator PMSM with separately controlled dual three-phase winding for eVTOL propulsion," *IEEE Trans. Transp. Electrific.*, vol. 8, no. 4, pp. 4255–4264, Dec. 2022.

[5] H. S. Che, E. Levi, M. Jones, M. J. Duran, W.-P. Hew, and N. A. Rahim, "Operation of a six-phase induction machine using series-connected machine-side converters," *IEEE Trans. Ind. Electron.*, vol. 61, no. 1, pp. 164–176, Jan. 2014.

[6] I. Zoric, M. Jones, and E. Levi, "Arbitrary power sharing among three-phase winding sets of multiphase machines," *IEEE Trans. Ind. Electron.*, vol. 65, no. 2, pp. 1128–1139, Feb. 2018.

[7] M. J. Duran, I. González-Prieto, A. González-Prieto, and F. Barrero, "Multiphase energy conversion systems connected to microgrids with unequal power-sharing capability," *IEEE Trans. Energy Convers.*, vol. 32, no. 4, pp. 1386–1395, Dec. 2017.

[8] S. Hu, M. Xiong, Z. Liang, and X. He, "Torque distributed control strategy for the dual three-phase PMSM in hybrid energy storage system application," *IEEE Trans. Ind. Electron.*, vol. 67, no. 4, pp. 2544–2552, Apr. 2020.

[9] F. Luise, S. Pieri, M. Mezzarobba, and A. Tessarolo, "Regenerative testing of a concentrated-winding permanent-magnet synchronous machine for offshore wind generation—Part I: Test concept and analysis," *IEEE Trans. Ind. Appl.*, vol. 48, no. 6, pp. 1779–1790, Nov./Dec. 2012.

[10] A. A. Abduallah, O. Dordevic, M. Jones, and E. Levi, "Regenerative test for multiple three-phase machines with even number of neutral points," *IEEE Trans. Ind. Electron.*, vol. 67, no. 3, pp. 1684–1694, Mar. 2020.

[11] S. Rubino, O. Dordevic, E. Armando, I. R. Bojoi, and E. Levi, "A novel matrix transformation for decoupled control of modular multiphase PMSM drives," *IEEE Trans. Power Electron.*, vol. 36, no. 7, pp. 8088–8101, Jul. 2021.

[12] Y. Hu, Z. Q. Zhu, and M. Odavic, "Comparison of two-individual current control and vector space decomposition control for dual three-phase PMSM," *IEEE Trans. Ind. Appl.*, vol. 53, no. 5, pp. 4483–4492, Sep./Oct. 2017.

[13] Y. Zhao and T. A. Lipo, "Space vector PWM control of dual three-phase induction machine using vector space decomposition," *IEEE Trans. Ind. Appl.*, vol. 31, no. 5, pp. 1100–1109, Sep./Oct. 1995.

[14] I. Zoric, M. Jones, and E. Levi, "Arbitrary *d–q* current sharing in three-phase winding sets of multi-phase machines," *J. Eng.*, vol. 2019, no. 17, pp. 4173–4177, Jun. 2019.

[15] X. Wang, Z. Wang, and Z. Xu, "A hybrid direct torque control scheme for dual three-phase PMSM drives with improved operation performance," *IEEE Trans. Power Electron.*, vol. 34, no. 2, pp. 1622–1634, Feb. 2019.

[16] S. M. Suhel and R. Maurya, "Realization of 24-sector SVPWM with new switching pattern for six-phase induction motor drive," *IEEE Trans. Power Electron.*, vol. 34, no. 6, pp. 5079–5092, Jun. 2019.

[17] K. Marouani, L. Baghli, D. Hadiouche, A. Kheloui, and A. Rezzoug, "A new PWM strategy based on a 24-sector vector space decomposition for a six-phase VSI-fed dual stator induction motor," *IEEE Trans. Ind. Electron.*, vol. 55, no. 5, pp. 1910–1920, May 2008.

[18] S. Paul and K. Basu, "Overmodulation techniques of asymmetrical six-phase machine with optimum harmonic voltage injection," *IEEE Trans. Ind. Electron.*, vol. 68, no. 6, pp. 4679–4690, Jun. 2021.

[19] M. A. E., M. S. Shaikh, and R. Maurya, "Performance investigation on SVPWM sequences based on reduced common-mode voltage in dual three-phase asymmetrical machine," *IEEE Trans. Energy Convers.*, vol. 36, no. 4, pp. 2884–2893, Dec. 2021.

[20] K. Cui, C. Wang, M. Zhou, and S. Sun, "Comprehensive investigation of space-vector PWM including novel switching sequences for dual three-phase motor drives," *IEEE Trans. Transp. Electrific.*, vol. 9, no. 1, pp. 1350–1362, Mar. 2023.

[21] Z. Zhang, Z. Wang, X. Wei, Z. Liang, R. Kennel, and J. Rodriguez, "Space-vector-optimized predictive control for dual three-phase PMSM with quick current response," *IEEE Trans. Power Electron.*, vol. 37, no. 4, pp. 4453–4462, Apr. 2022.

[22] W. Liao, M. Lyu, S. Huang, Y. Wen, M. Li, and S. Huang, "An enhanced SVPWM strategy based on vector space decomposition for dual three-phase machines fed by two DC-source VSIs," *IEEE Trans. Power Electron.*, vol. 36, no. 8, pp. 9312–9321, Aug. 2021.

[23] G. Feng, C. Lai, W. Li, Z. Li, and N. C. Kar, "Dual reference frame based current harmonic minimization for dual three-phase PMSM considering inverter voltage limit," *IEEE Trans. Power Electron.*, vol. 36, no. 7, pp. 8055–8066, Jul. 2021.

[24] S. Liu, Z. Song, Y. Liu, Y. Chen, and C. Liu, "Flux-weakening controller design of dual three-phase PMSM drive system with copper loss minimization," *IEEE Trans. Power Electron.*, vol. 38, no. 2, pp. 2351–2363, Feb. 2023.

[25] J. Prieto, J. A. Riveros, and B. Bogado, "Multifrequency output voltage generation for asymmetrical dual three-phase drives," in *Proc. IEEE Int. Electric Machines Drives Conf.*, 2017, pp. 1–6.

[26] J. Xu, M. Odavic, Z.-Q. Zhu, Z.-Y. Wu, and N. M. A. Freire, "Modulation restraint analysis of space vector PWM for dual three-phase machines under vector space decomposition," *IEEE Trans. Power Electron.*, vol. 36, no. 12, pp. 14491–14507, Dec. 2021.
[27] K. Yu, Z. Wang, X. Wang, and Z. Zou, "An online flux estimation for dual three-phase SPMSM drives using position-offset injection," *IEEE Trans. Power Electron.*, vol. 36, no. 10, pp. 11606–11617, Oct. 2021.

Xiaochen Ma was born in Hebei, China, in 1995. He received the B.S. degree from Fuzhou University, Fuzhou, China, and the M.S. degree from Tianjin University, Tianjin, China, in 2018 and 2021, respectively, both in electrical engineering. He is currently working toward the Ph.D. degree in electrical engineering with Tianjin University, Tianjin, China.

His research interests include power converters and electric machine drives.

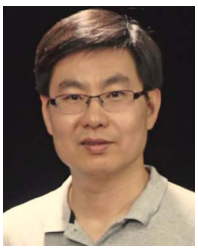

Bin Li was born in China, in 1976. He received the Ph.D. degree in electrical engineering from Tianjin University (TJU), Tianjin, China, in 2006.

From 2014 to 2015, he was a Visiting Scholar with the Department of Electrical Engineering and Computer Science, University of Central Florida, Orlando, FL, USA. He is currently a Professor with the School of Electrical and Information Engineering, TJU. His research interests include electric machine design and control.

Guidan Li was born in China, in 1975. She received the M.S. and Ph.D. degrees in electrical engineering from Tianjin University (TJU), Tianjin, China, in 2004 and 2009, respectively.

From March 2014 to March 2015, she was a Visiting Scholar with the University of Central Florida, Orlando, FL, USA. She is currently a Professor with the School of Electrical and Information Engineering, TJU. Her research interests include power electronics and their applications.

Qiaoman Zhu was born in Anhui, China, in 1999. She received the B.S. degree from Anhui University, Hefei, China, and the M.S. degree from Tianjin University, Tianjin, China, in 2020 and 2023, respectively, both in electrical engineering.

She is currently with the Jianghuai Advance Technology Center, Hefei, China. Her research interests include fault-tolerant control of multiphase motors, pulsewidth modulation, and harmonic analysis of multiphase converters.